



HAL
open science

Spatiotemporal organization of human sensorimotor beta burst activity

Catharina Zich, Andrew J Quinn, James J Bonaiuto, George O’neill, Lydia C
Mardell, Nick S Ward, Sven Bestmann

► **To cite this version:**

Catharina Zich, Andrew J Quinn, James J Bonaiuto, George O’neill, Lydia C Mardell, et al.. Spatiotemporal organization of human sensorimotor beta burst activity. 2022. hal-03868894v1

HAL Id: hal-03868894

<https://hal.science/hal-03868894v1>

Preprint submitted on 24 Nov 2022 (v1), last revised 22 Nov 2023 (v2)

HAL is a multi-disciplinary open access archive for the deposit and dissemination of scientific research documents, whether they are published or not. The documents may come from teaching and research institutions in France or abroad, or from public or private research centers.

L’archive ouverte pluridisciplinaire **HAL**, est destinée au dépôt et à la diffusion de documents scientifiques de niveau recherche, publiés ou non, émanant des établissements d’enseignement et de recherche français ou étrangers, des laboratoires publics ou privés.

1 **Spatiotemporal organization of human sensorimotor beta burst activity**

2 Catharina Zich^{1,2}, Andrew J Quinn³, James J Bonaiuto^{4,5}, George O'Neill⁶, Lydia C Mardell¹,
3 Nick S Ward¹, Sven Bestmann^{1,6}

4

5

6 Affiliations:

7 1) Department of Clinical and Movement Neuroscience, UCL Queen Square Institute of
8 Neurology, London, UK

9 2) Wellcome Centre for Integrative Neuroimaging, FMRIB, Nuffield Department of Clinical
10 Neurosciences, University of Oxford, Oxford, UK

11 3) Oxford Centre for Human Brain Activity, Wellcome Centre for Integrative Neuroimaging,
12 Department of Psychiatry, University of Oxford, Oxford, UK

13 4) Institut des Sciences Cognitives Marc Jeannerod, CNRS UMR 5229, Bron, France

14 5) Université Claude Bernard Lyon 1, Université de Lyon, France

15 6) Wellcome Centre for Human Neuroimaging, UCL Queen Square Institute of Neurology,
16 London, UK

17

18

19 Keywords:

20 Beta burst, Sensorimotor cortex, Traveling wave, oscillation,

21

22 Word count:

23 Figure count: 5

24

25 **Abstract**

26 Beta oscillations in human sensorimotor cortex are hallmark signatures of healthy and
27 pathological movement. In single trials, beta oscillations include bursts of intermittent,
28 transient periods of high-power activity. These burst events have been linked to a range of
29 sensory and motor processes, but their precise spatial, spectral, and temporal structure
30 remains unclear. Specifically, a role for beta burst activity in information coding and
31 communication suggests spatiotemporal patterns, or travelling wave activity, along specific
32 anatomical gradients. We here show in human magnetoencephalography recordings that
33 burst activity in sensorimotor cortex occurs in planar spatiotemporal wave-like patterns that
34 dominate along two axes either parallel or perpendicular to the central sulcus. Moreover, we
35 find that the two propagation directions are characterised by distinct anatomical and
36 physiological features. Finally, our results suggest that sensorimotor beta bursts occurring
37 before and after a movement share the same generator but can be distinguished by their
38 anatomical, spectral and spatiotemporal characteristics, indicating distinct functional roles.

39 **Introduction**

40 Neural activity at the rate of 13-30Hz constitute one of the most prominent
41 electrophysiological signatures in the sensorimotor system (Baker, 2007; Brown, 2007). This
42 sensorimotor beta activity is traditionally seen to reflect oscillations: sustained rhythmic
43 synchronous spiking activity within neural populations. However, a substantial proportion of
44 sensorimotor beta activity occurs in bursts of intermittent, transient periods of synchronous
45 spiking activity (Jones, 2016) which relate to both motor, perceptual and sensory function
46 (Enz et al., 2021; Feingold et al., 2015; Heideman et al., 2020; Sherman et al., 2016; Shin et
47 al., 2017; Sporn et al., 2020; Tinkhauser, Pogosyan, Little, et al., 2017; Wessel, 2020; Zich et
48 al., 2018) and pathophysiological movement (Cagnan et al., 2019; Deffains et al., 2018;
49 Tinkhauser, Pogosyan, Little, et al., 2017; Tinkhauser, Pogosyan, Tan, et al., 2017), but their
50 functional role remains unclear.

51
52 Sensorimotor beta burst activity is commonly considered as zero-lagged (or standing wave)
53 activity which is generated by the summation of synchronized layer-specific inputs within
54 cortical columns that result in a cumulative dipole with a stereotypical wavelet shape in the
55 time domain (Bonaiuto et al., 2021; Law et al., 2022; Neymotin et al., 2020). These time-
56 periods of synchronous activity which generate standing wave activity are thought to convey
57 little information encoding (Brittain & Brown, 2014; Carhart-Harris, 2018; Carhart-Harris et
58 al., 2014). This view sides with the proposed akinetic role of high sensorimotor beta states
59 (Gilbertson et al., 2005; Joundi et al., 2012; Khanna & Carmena, 2017; Pogosyan et al., 2009).
60 However, burst activity may have heterogenous and mechanistically distinct components
61 which can be characterised by their distinct spatial, temporal, and spectral structure (Law et
62 al., 2022; Zich et al., 2020) that, in addition to zero-lagged activity, contains spatiotemporal
63 gradients, or travelling wave, components.

64
65 In animals, for example, a high proportion of sensorimotor beta activity occurs as travelling
66 waves (Rubino et al., 2006; Rule et al., 2018), in addition to highly synchronous standing
67 waves. In travelling waves, the relative timing of fluctuations of synchronous spiking activity
68 is not precisely zero-lagged but adopts a phase offset and moves across space. Propagation
69 of neural activity constitutes one mechanism for cortical information transfer and traveling

70 waves have been described over spatial scales that range from the mesoscopic (single cortical
71 areas and millimetres of cortex) to the macroscopic (global patterns of activity over several
72 centimetres) and extend over temporal scales from tens to hundreds of milliseconds
73 (Alexander et al., 2019; Davis et al., 2021; Heitmann et al., 2017; Muller et al., 2018; Roberts
74 et al., 2019; Rule et al., 2018).

75
76 Characterising traveling wave components within sensorimotor beta burst activity is of
77 relevance as it would provide insights into the putative underlying mechanisms and functional
78 roles of sensorimotor beta activity. For instance, in general terms, spatiotemporal
79 propagation of high amplitude beta may support information transfer across space and may
80 reflect the spatiotemporal patterns of sequential activation required for movement initiation
81 (Best et al., 2016; Rubino et al., 2006). At the macro-scale level, the specific propagation
82 properties, such as propagation direction and speed, may provide further constraints for the
83 putative functional role of burst activity in organizing behaviour across different brain regions
84 (Ding & Ermentrout, 2021), including the modulation of neural sensitivity (Davis et al., 2020)
85 or the sequencing of muscle representations in motor cortex (Muller et al., 2018; Riehle et
86 al., 2013; Takahashi et al., 2015). In humans, the precise properties of beta bursts, and
87 whether their high amplitude activity comprise distinct spatiotemporal gradients remains
88 unclear.

89
90 To address this, we here employed high signal-to-noise (SNR) magnetoencephalography
91 (MEG) in healthy human subjects during simple visually-cued motor behaviour. We show that
92 beta burst activity in sensorimotor cortex occurs in planar spatiotemporal wave-like patterns
93 that dominate along two anatomical axes. Crucially, our results show structure beyond the
94 inherent limitations of source reconstruction such as volume conduction or the spatial
95 pattern of beamformer weights. Moreover, we find that the two propagation directions are
96 characterised by distinct anatomical and physiological features. Finally, our results suggest
97 that sensorimotor beta bursts occurring before and after a movement share the same
98 generator but can be distinguished by their anatomical, spectral and spatiotemporal
99 characteristics, indicating distinct functional roles.

100

101 **Results**

102 **Temporal, spectral and spatial burst characteristics**

103 Participants completed three blocks per recording session, and 1-5 sessions on different days.
104 We analysed 123-611 trials per participant ($M = 438.5$, $SD = 151.0$ across individuals) in which
105 correct key presses were made with either the right index or middle finger, in response to
106 congruent imperative stimuli and high coherence visual cues (Bonaiuto et al., 2018; Little et
107 al., 2019). We focussed on these trial-types to delineate the multi-dimensional (temporal,
108 spectral, spatial) properties of sensorimotor beta burst activity (**Fig. 1a,b**; (Zich et al., 2020)).
109 Bursts were identified over a 4 second time window (-2 to 2s relative to the button press), in
110 the beta frequency range (13 to 30Hz) and a region-of-interest (ROI) spanning the primary
111 motor cortex (M1) and adjacent areas of the primary sensory cortex and premotor cortex
112 using session-specific amplitude thresholding ((Little et al., 2019); **Supplemental Fig. 1**;
113 **Supplemental Fig. 2**) and 5D clustering.

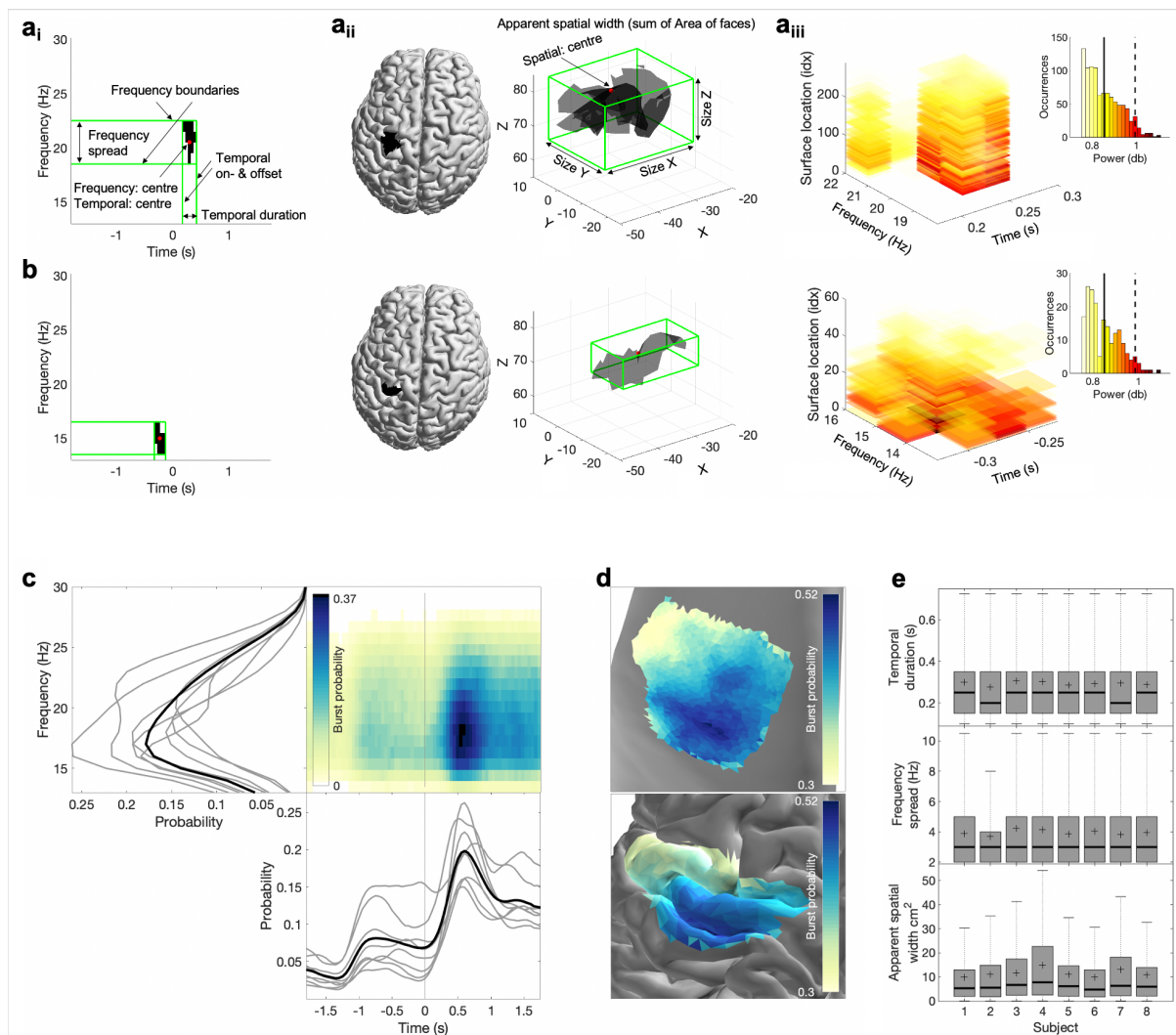
114
115 In the temporal domain, we observed the expected increase in burst probability post-vs pre-
116 movement (**Fig. 1c**). Burst duration was consistent across subjects ($M = 238\text{ms}$, $SD = 23\text{ms}$
117 across individuals, temporal resolution 50ms, **Fig. 1e**). Spectrally, while beta bursts occurred
118 throughout the beta frequency range, most bursts were identified in the lower beta
119 frequency range (**Fig. 1c**), with a consistent frequency spread across subjects ($M = 3\text{Hz}$, $SD =$
120 0Hz across individuals, frequency resolution 1Hz, **Fig. 1e**). To examine burst probability as a
121 function of space across subjects, individual subject maps were spatially normalised,
122 projected onto a single surface, and then averaged across subjects. Topographically, bursts
123 were most likely to occur in M1 (**Fig. 1d**, see **Supplemental Fig. 3** for individual subject maps)
124 and spanned, on average, 10% of the ROI's surface area ($M = 6\text{cm}^2$; $SD = 0.9\text{cm}^2$ across
125 individuals).

126
127 We performed a range of control analyses to examine whether our results can be explained
128 by trivial properties of the beamformer itself. Firstly, we sought to assess whether differences
129 in the bursts' apparent spatial width could be explained by differences in SNR across and/or
130 within sessions rather than differences in the spatial distribution of cortical activity. We
131 reasoned that if differences in SNR across sessions would explain bursts' apparent spatial

132 width, then burst amplitude and burst apparent spatial width should be negatively correlated
133 (for a schematic illustration see **Supplemental Fig. 4ai**). The absence of significant correlations
134 between burst amplitude and burst apparent spatial width, both across sessions within
135 subjects and also across sessions and individuals (**Supplemental Fig. 4aii**), suggests that the
136 apparent spatial width of bursts is not solely explained by differences in SNR across sessions,
137 and across individuals.

138 Further we reasoned that if the apparent spatial width is driven by differences in SNR across
139 bursts within a session, then a positive relationship between burst amplitude and burst
140 apparent spatial width within sessions should be present, and there should be no systematic
141 phase differences across different spatial locations within each burst (for a schematic
142 illustration see **Supplemental Fig. 4b**). While burst amplitude and burst apparent spatial
143 width are positively correlated within sessions (Pearson's r : $M = 0.749$, $SD = 0.056$ across
144 sessions, all p 's < 0.001), we consistently observed diverse phase lags across space within
145 these bursts (see results section: **Sensorimotor burst activity propagates along two axes**),
146 which are unlikely to arise simply from amplitude scaling of a single source.

147 Together, these control analyses suggest that differences in bursts' apparent spatial width is
148 not merely due to differences in SNR across and/or within sessions, but for the most part due
149 to differences in the spatial distribution of cortical activity.



150

151 **Fig. 1: Spectral, temporal, and spatial beta burst characteristics.**

152 (a) Burst characteristics for a single example burst. (a_i) Temporal and spectral burst characteristics. (a_{ii}) Spatial
 153 burst characteristics. (a_{iii}) Burst amplitude. Shown is the amplitude for each temporal, spectral and spatial
 154 location of that burst as well as the histogram across all three signal domains. Often the mean (straight line) or
 155 the 95 percentile (dashed line) is used as burst amplitude.

156 (b) Same as (a) for a different burst.

157 (c) Burst probability as a function of time and frequency across all bursts of all subjects (see **Supplemental Fig. 3**
 158 for individual subjects). Burst probability as a function of time (bottom) and frequency (left) is shown for each
 159 subject separately (grey lines) and across subjects (black line).

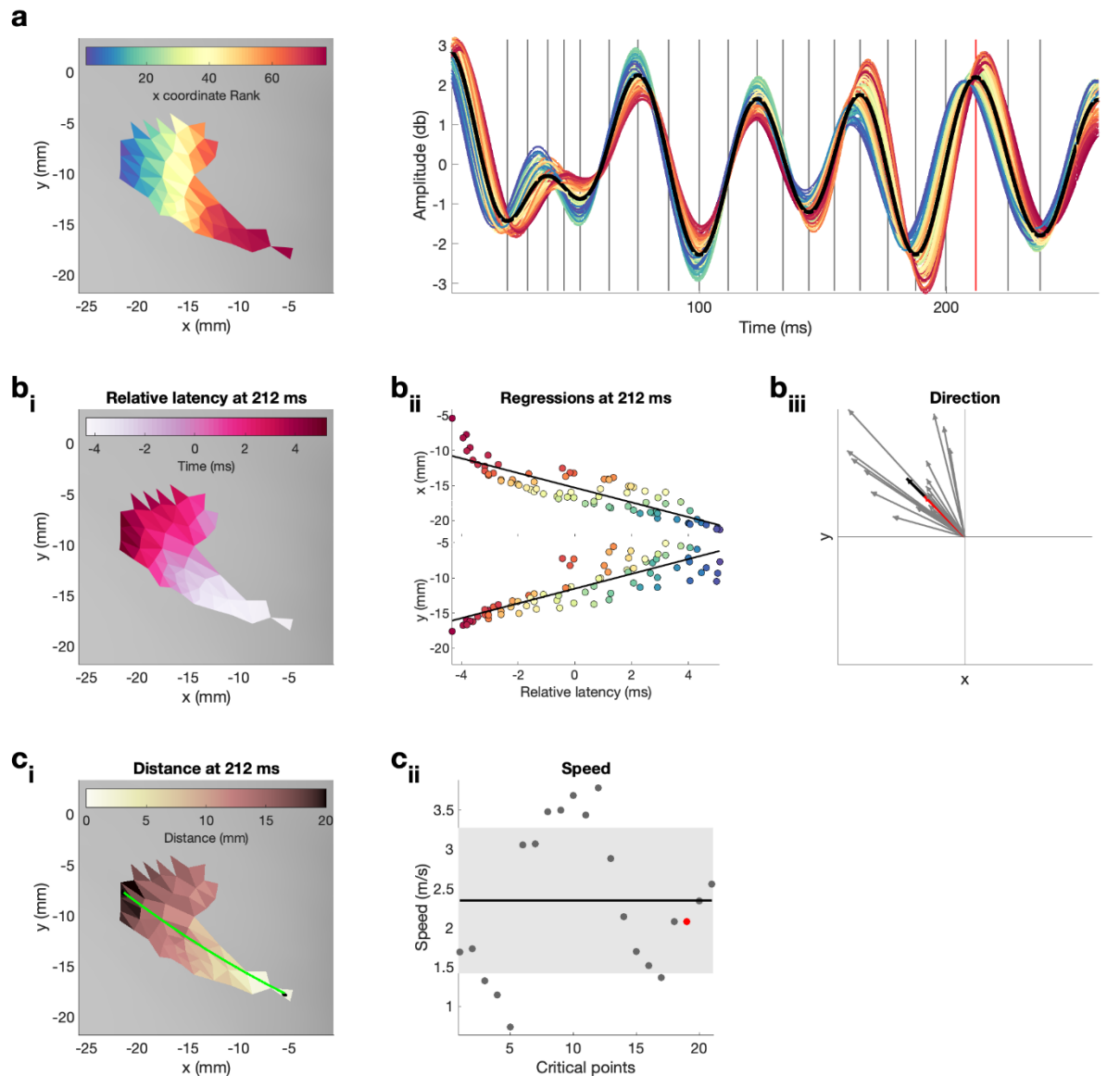
160 (d) Burst probability as a function of space across all bursts of all subjects on the inflated surface (top) and original
 161 surface (bottom). To visualise burst probability as a function of space across subjects, individual subject maps
 162 were spatially normalised, projected onto a single surface, and then averaged across subjects. **Supplemental Fig.**
 163 **3** depicts the burst probability for each subject in native space.

164 (e) Burst temporal duration (top), frequency spread (middle) and apparent spatial width (bottom) for each
 165 subject as boxplot.

166 **Sensorimotor beta burst activity is propagating**

167 The precise decomposition of beta bursts into their spectral, spatial, and temporal signal
168 domains allowed us to next assess any spatiotemporal gradients within sensorimotor beta
169 bursts. For each burst, we identified the dominant propagation direction and propagation
170 speed (**Supplemental Fig. 1**). Propagation direction and speed were estimated from critical
171 points in the oscillatory cycle (**Fig. 2a**) and then averaged across critical points within one
172 burst. The propagation direction at each critical point was estimated from the relative latency
173 (**Fig 2bi**). Next, the propagation direction was estimated, using linear regression
174 (Balasubramanian et al., 2020), whereby the relative latency at the surface location was
175 predicted from the coordinates of the surface location of the inflated surface. We excluded
176 complex spatiotemporal patterns such as random or circular patterns (**Supplemental Fig.**
177 **5b,c**; $M = 8.25\%$, $SD = 0.88\%$ across individuals; (Denker et al., 2018; Rule et al., 2018)), to
178 focus on bursts with a dominant planar propagation orientation (**Supplemental Fig. 5a**; $M =$
179 79.6% , $SD = 2.4\%$ across individuals; (Balasubramanian et al., 2020; Rubino et al., 2006;
180 Takahashi et al., 2011)).

181
182 To test whether the planar spatiotemporal structure of bursts is significant we compared the
183 propagation properties detected in real burst activity to those of surrogate data for a subset
184 of 100 randomly selected bursts. For each burst, 1000 phase-randomised surrogates (cf.
185 Hurtado et al., 2004) were created and the propagation properties of the real data were
186 compared to their distribution from 1000 surrogates. Real sensorimotor beta burst activity
187 exhibited significantly stronger planar spatiotemporal structure than spectrally matched
188 surrogate data (all 100 bursts $p < 0.01$).



189
 190 **Fig. 2: Quantification of propagation direction and propagation speed on one exemplar burst.**
 191 For a dynamic version, i.e., updated for each critical point, see Supplemental Video 1.
 192 (a) Left: Single burst on inflated surface. Spatial locations are colour-coded by their x coordinate rank. Right:
 193 Neural activity in the beta range (13-30 Hz) from each surface location for the temporal duration of the burst.
 194 Vertical lines indicate critical points (four critical points per oscillatory cycle, i.e., peak and trough as well as
 195 peak-trough and trough-peak midpoint) at which propagation direction and propagation speed were
 196 estimated. Red vertical line indicates the control point at 212ms, shown in (b_{i,iii}) and (c_{i,ii}), and highlighted in (b_{iii})
 197 and (c_{iii}).
 198 (b_i) Relative latencies of the critical point at 212ms as a function of space illustrated on inflated surface.
 199 (b_{ii}) Simple linear regressions between latency at surface location and x (top) as well as y (bottom) coordinates
 200 of the surface location for the critical point at 212ms. Colour refers to the x coordinate rank as illustrated in (a).
 201 (b_{iii}) Propagation direction obtained from regression coefficients for each critical point (grey), the critical point
 202 at 212ms (red) and the average across all critical points (black, i.e., propagation direction of burst).
 203 (c_i) Distance, i.e., exact geodesic distance, from the surface location with the smallest relative latency to each
 204 surface location on the inflated surface for the critical point at 212ms. Green line indicated the path, i.e.,
 205 distance, from the surface location with the smallest to the surface location with the largest relative latency.
 206 (c_{ii}) Propagation speed for each critical point (grey), the critical point at 212ms (red). The standard deviation
 207 across critical points is indicated by the grey area and the average across all critical points (i.e., propagation
 208 speed of burst) is indicated by the black horizontal line.
 209

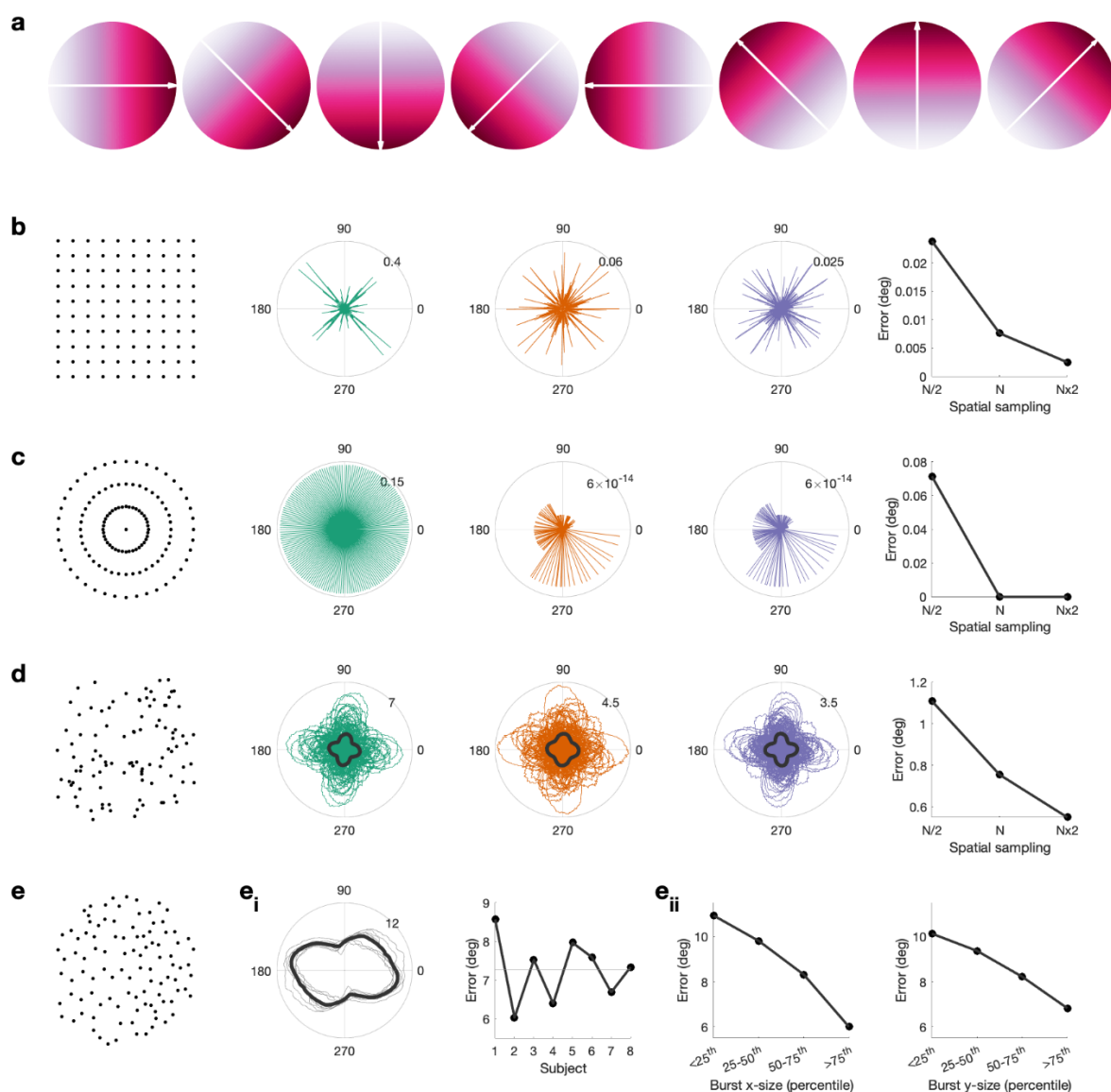
210 Accuracy of the propagation direction estimation in simulated and surface meshes

211 Before assessing the propagation direction of sensorimotor beta burst activity, we evaluated
212 the accuracy of the propagation direction estimation. To this end, we created 360 noise free
213 high-resolution gradients spanning 1deg-360deg (in steps of 1deg; subset shown in **Fig. 3a**).
214 The propagation direction of these gradients was then estimated from three different 2D
215 surface mesh types (square mesh, circular mesh, random mesh; **Fig. 3b-d**) and three spatial
216 sampling rates ($N/2$, N , $N \times 2$, whereby N approximates the spatial sampling of the real mesh).
217 By comparing the true and estimated propagation direction we found that under noise free
218 conditions, the propagation direction can be estimated accurately from regular meshes (**Fig.**
219 **3b,c**), whereas the mean error is roughly twice as large for random meshes (**Fig. 3d**).
220 This is relevant because the surface mesh obtained from brain imaging data is irregular. When
221 evaluating the accuracy of the propagation direction estimates using the real mesh (**Fig. 3e**)
222 and the real spatial burst properties, we found an average error of 7deg between true and
223 estimated propagation direction, with little variability across individuals ($SD = 0.5\text{deg}$ across
224 subjects) and angles ($SD = 1.5\text{deg}$ across angles; **Fig. 3e_i**). Across individuals the error was
225 smallest for gradient directions around 104/284deg and largest around 170/350deg (**Fig. 3e_i**).
226 Further, for bursts with a larger apparent spatial width (i.e., containing more spatial samples),
227 the estimated error is lower (**Fig. 3e_{ii}**).

228

229 Overall, these results suggest that propagation directions can be estimated with sufficient
230 accuracy from higher SNR MEG recordings over a relatively small cortical patch, as here.

231



232
233
234
235
236
237
238
239
240
241
242
243
244
245
246

Fig. 3: Propagation direction can be estimated accurately from cortical meshes.

(a) Simulated gradient at 0, 45, 90, 135, 180, 225 and 270 degrees.
 (b) Error between simulated gradient and estimated gradient on a square mesh. We test three different spatial sampling rates, $N/2$ (green), N (red) and $N \times 2$ (blue), whereby the spatial sampling of N is roughly equivalent to the spatial sampling of the inflated surface. Error is calculated for 1-360deg in steps of 1deg. The median error per spatial sampling is shown in the right, i.e., higher spatial sampling results in a lower error.
 (c) As (b), but for a circular mesh.
 (d) Error between simulated gradient and estimated gradient on a random mesh. 100 random meshes were generated. The error for each iteration is shown as well as the mean across iterations (black line).
 (e) Error between simulated gradient and estimated gradient on the inflated surface. The error was calculated for each burst. (ei) The mean across bursts is shown for each subject (grey lines) and across subjects (black line). For each subject the mean error across all angles and bursts is shown, i.e., error is comparable across subjects. (eii) Error as a function of burst size along the x-axis (left) and y-axis (right), i.e., the error is lower in bigger burst.

247 **Sensorimotor burst activity propagates along two axes**

248 Having established that the spatial sampling of the cortical mesh is sufficient to detect
249 propagation in simulated gradients, we analysed the propagation properties of the
250 sensorimotor beta burst activity. We observed that neural activity within beta bursts
251 propagates along two dominant axes, which were approximately 90deg apart (**Fig. 4a**): one
252 anterior-posterior (a-p) axis traversing the central sulcus in approximately perpendicular
253 fashion, and one medial-lateral (m-l) axis running approximately parallel to (i.e., along) the
254 central sulcus. The propagation distributions along these axes were well described by a
255 mixture of four von Mises functions with means of 66deg and 248deg for the a-p axis, and
256 means of 142deg and 324deg for the m-l axis, indicating that the surface mesh imposes
257 structure. Note, however, that these axes do not align with the directions showing the
258 smallest or the largest error when estimating the direction from noise-free gradients on the
259 same surface mesh and spatial burst properties, indicating that the mesh properties do not
260 drive the observed propagation direction.

261
262 The reliability of von Mises functions was assessed using a split-half reliability test. 500 split
263 halves were computed and four von Mises functions estimated on each half independently.
264 The length and direction of the von Mises functions were highly reproducible for all four von
265 Mises functions across both halves of the data (percentage difference in length: $M = 4.32\%$,
266 $SD = 3.86\%$; angular difference: $M = 2.2\text{deg}$, $SD = 2.8\text{deg}$; across 500 repetitions and four von
267 Mises functions; **Supplemental Fig. 6**). Further, we tested whether the four von Mises
268 functions were significantly different from zero using non-parametric permutation testing.
269 5000 permutations were carried out by randomising the propagation direction of each burst
270 and estimating four von Mises functions of the distribution of all bursts. The length of the real
271 van Mises functions were significant while correcting for multiple comparison at $p < 0.01$.

272
273 Finally, to examine whether the two main propagation axes can be trivially explained by
274 spatial variability in the beamformer weights, we correlated the latency of the critical points
275 across space before and after regressing out the main components of the spatial variability in
276 the LCMV weights. We found significant correlations (Pearson's r : $M = 0.61$, $SD = 0.27$ years
277 across individuals, all p 's < 0.05), indicating that beamformer weights contribute to, but do
278 not solely explain the observed propagation directions.

279

280 Together, these results demonstrates that propagation of sensorimotor beta burst activity
281 propagation occurs along two, orthogonal axes which are oriented approximately parallel and
282 perpendicular the CS.

283

284 **Burst characteristics differ as function of the propagation axis**

285 The aforementioned analyses suggest that burst activity propagates along one of two
286 propagation axes. We next asked whether burst propagating along these distinct axes vary in
287 their physiological properties. Specifically, we tested for potential differences in the temporal
288 (i.e., temporal centre), spectral (i.e., frequency centre), or spatial domain (spatial location),
289 as well as burst extent, burst amplitude and propagation speed.

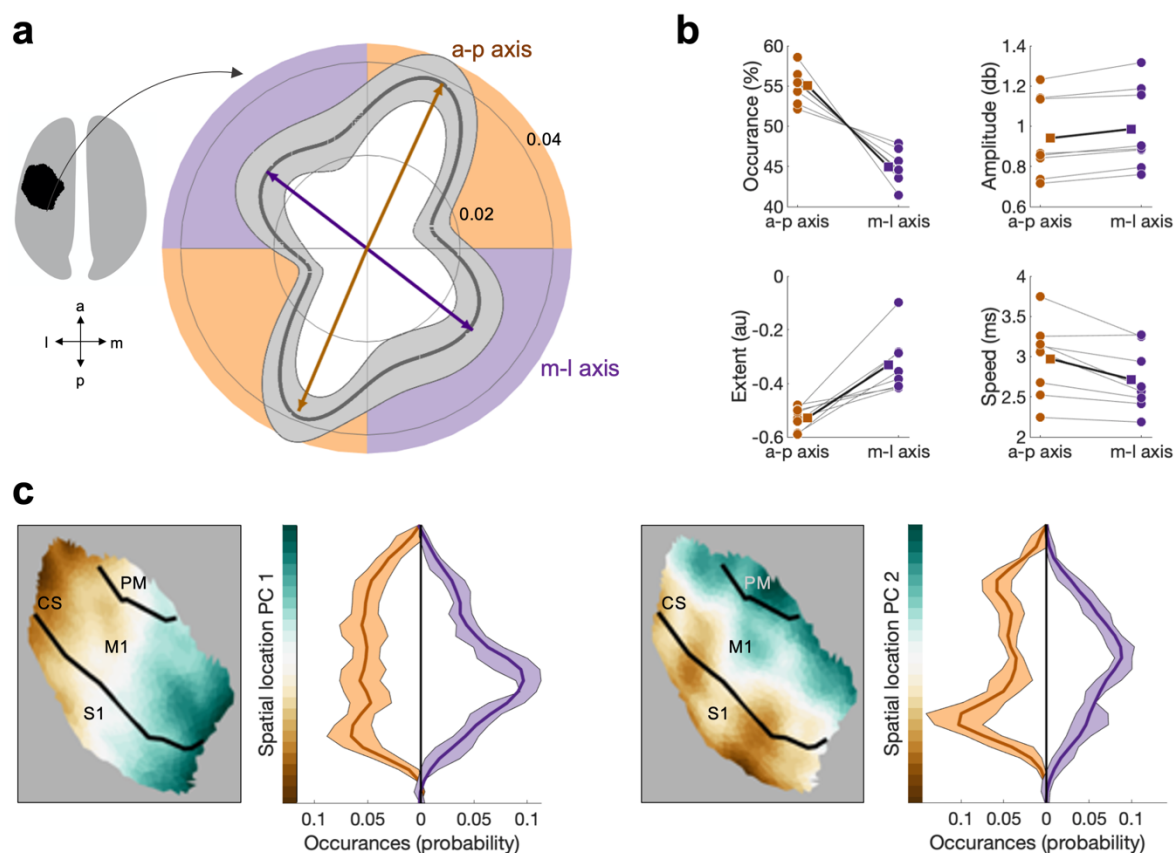
290

291 We found significantly more bursts propagating along the a-p axis ($M = 55.1\%$, $SD = 2.0$ across
292 individuals), compared to the m-l axis ($M = 44.9$, $SD = 2.0$ across individuals; T [test statistic
293 for Wilcoxon signed-rank test, see **Statistical analysis**] = 2.521, $p < 0.012$; **Fig. 4b**). Moreover,
294 bursts propagating along these axes differ in their amplitude, extent, speed (**Fig. 4b**) and
295 spatial location (**Fig. 4c**). Specifically, burst propagating anterior-posterior are characterised
296 by a higher burst amplitude (a-p $M = 0.94$, $SD = 0.20$ across individuals; m-l: $M = 0.98$, $SD =$
297 0.20 across individuals; $T = 2.521$, $p < 0.012$), larger extent (a-p: $M = -0.53$, $SD = 0.04$ across
298 individuals; m-l: $M = -0.33$, $SD = 0.1$ across individuals; $T = 2.521$, $p < 0.012$) and slower
299 propagation speeds (a-p: $M = 2.97\text{m/s}$, $SD = 0.47\text{m/s}$ across individuals; m-l: $M = 2.72\text{m/s}$, SD
300 $= 0.40\text{m/s}$ across individuals; $T = 2.38$, $p < 0.017$).

301

302 The notion that burst activity propagates along distinct anatomical axes was further
303 supported by differences in the spatial location of bursts propagating along these axes.
304 Specifically, the distribution of spatial location PC1 and PC2 (see methods section: **Burst**
305 **characteristics; Supplemental Fig. 7**) differed significantly for burst propagating along axis m-
306 l, relative to bursts propagating along axis a-p for both PC1 (KS [test statistic for Kolmogorov-
307 Smirnov test, see **Statistical analysis**]: $M = 0.182$ across individuals, range = 0.107 – 0.232; 8/8
308 p 's < 0.001) and PC2 (KS: $M = 0.203$ across individuals, range = 0.110 – 0.253; 8/8 p 's < 0.001 ;
309 **Fig. 4c**). This indicates that bursts propagating along a-p are located predominantly in the

310 putative hand region of M1 in the vicinity of the central sulcus, whereas the central locus of
 311 burst activity propagating medio-laterally is in S1.



312

313 **Fig. 4: Beta bursts activity propagates along two axes, which have distinct bursts properties.**

314 (a) Polar probability histograms showing the probability distribution of burst direction in MNI space. Probability
 315 distributions were calculated for each subject individually and then averaged (dark grey line). Variance across
 316 subjects is expressed as standard deviation from the mean (light grey area). To estimate the dominant
 317 propagation directions, a mixture of von Mises functions was fitted to the averaged probability distribution
 318 (arrows). The four functions lie on two axes. One axis has an anterior-posterior orientation which is
 319 approximately perpendicular to the orientation of the central sulcus (a-p), while the other axis runs in
 320 approximately medial-lateral orientation which is approximately parallel to the orientation of the central sulcus
 321 (m-l).

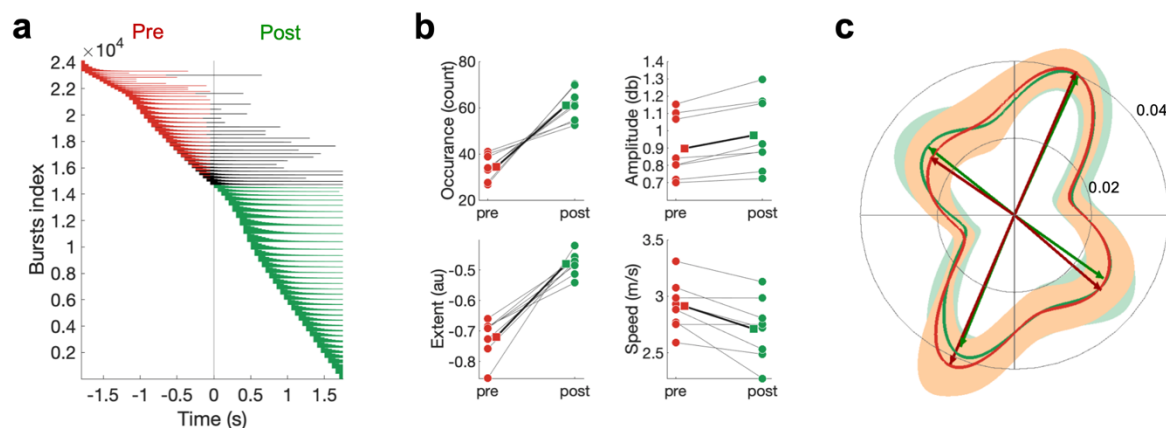
322 (b) Burst occurrence, burst amplitude, burst extent, and burst speed differ as a function of propagation direction.
 323 Medians are shown for each subject (circles) and the mean across the subjects' medians (square).

324 (c) Burst location differs as a function of burst direction. Burst location is described by two Principal
 325 Components (PCs) of the Cartesian coordinates of the centre of the burst. For each of the two PCs the surface
 326 plot of the component structure and the probability distributions of the PC score are shown. Probability
 327 distributions were calculated for each subject individually and then averaged (dark line). Variance across
 328 subjects is expressed as standard deviation from the mean (light area). Bursts with a direction parallel to the
 329 CS, relative to bursts with a direction perpendicular to the CS, are located more centrally in the ROI. CS, Central
 330 Sulcus. S1, Primary Sensory Cortex. M1, Primary Motor Cortex. PM, Premotor Cortex.

331 **Distinct physiological fingerprints of pre- and post-movement bursts**

332 Having established that sensorimotor burst activity propagates along two major axes, with
333 distinct foci of burst activation for burst activity propagating along these, we turned to the
334 question whether bursts occurring pre- or post-movement might also be distinguished by
335 their burst and/or propagation properties. To this end, we defined pre-movement bursts as
336 bursts with an on- and offset prior to the movement, and post-movement bursts as bursts
337 with an on- and offset post movement (**Fig. 5a**). Bursts with an onset pre-movement and
338 offset post- movement ($M = 4.7\%$, $SD = 1.9\%$ across individuals) are excluded from this specific
339 analysis. As expected, we found significantly more bursts post- than pre-movement (pre: $M =$
340 34.3% , $SD = 5.3\%$ across individuals; post: $M = 60.9$, $SD = 6.9\%$ across individuals; $T = 2.521$, p
341 $= 0.012$; **Fig. 5b**). Further post-movement bursts are characterised by a larger amplitude (pre:
342 $M = 0.898\text{db}$, $SD = 0.181\text{db}$ across individuals; post: $M = 0.974\text{db}$, $SD = 0.208\text{db}$ across
343 individuals; $T = 2.521$, $p = 0.012$; **Fig. 5b**) and were generally larger in all signal dimensions
344 (burst extent; pre: $M = -0.719$, $SD = 0.063$ across individuals; post: $M = -0.480$, $SD = 0.036$
345 across individuals; $T = 2.521$, $p = 0.012$; **Fig. 5b**). However, the average spatial location and
346 frequency centre were not significantly different between pre- and post-movement bursts
347 (all p 's > 0.1 ; **Supplemental Fig. 8**).

348
349 Further, in line with non-human primate recordings (Rubino et al., 2006), propagation
350 directions were not significantly different between pre- and post-movement bursts (U^2 [test
351 statistic for Watson's U^2 test, see **Statistical analysis**]: $M = 0.088$ across individuals, range =
352 $0.025 - 0.190$; $8/8$ p 's > 0.1 ; **Fig. 5c**). The directions of pre-movement bursts activity
353 propagating along the a-p ($68/246\text{deg}$) and m-l direction ($148/315\text{deg}$) did not differ from the
354 directions observed post-movement (a-p: $66/248\text{deg}$; m-l: $142/325\text{deg}$). However, while the
355 mean propagation direction did not differ between pre- and post-movement bursts, we found
356 that propagation speed for post-movement bursts was significantly slower than pre-
357 movement (pre: $M = 2.90\text{m/s}$, $SD = 0.20\text{m/s}$ across individuals; post: $M = 2.69$, $SD = 0.28$
358 across individuals; $T = 2.521$, $p = 0.012$; **Fig. 5b**). Finally, we sought to explore whether pre-
359 movement burst characteristics are related to reaction time. We did not find evidence that
360 burst characteristics relate to reaction time in these data (all p 's > 0.1).



361
362

Fig. 5: Differences in pre- and post-movement beta bursts.

363 (a) Burst timing relative to the button press across all subjects. Each horizontal line represents one burst. Bursts
364 are sorted by burst onset and burst duration using multiple-level sorting, yielding the burst index. Pre-movement
365 bursts (i.e., bursts that start and end prior to the button press) are highlighted in red, post-movement bursts (i.e.,
366 bursts that start after the button press) are highlighted in green, and bursts that start prior to the button press
367 and end after the button press are highlighted in black.

368 (b) Number of bursts, burst amplitude, burst extent and burst speed differ between pre- and post-movement
369 bursts. Medians are shown for each subject (circles) and the mean across the subjects' medians (square).

370 (c) Propagation direction does not differ between pre- and post- movement bursts. Shown are polar probability
371 histograms separately for pre- and post- movement bursts. Probability distributions were calculated for each
372 subject individually and then averaged (dark line). Variance across subjects is expressed as standard deviation
373 from the mean (light area). Von Mises functions were fitted separately for pre- and post-movement bursts.

374 **Discussion**

375 The temporal, spectral, and spatial characteristics of beta bursts in human sensorimotor
376 cortex remain unknown. We here show that beta bursts in human sensorimotor cortex occur
377 predominantly post-movement, in the lower beta frequency band, and on the posterior bank
378 of the precentral gyrus. Crucially, sensorimotor beta bursts do not just occur as local standing
379 waves of synchronous activity but propagate along one of two axes that run parallel or
380 perpendicular to the central sulcus, respectively. In addition to the principal axis of their
381 propagation direction, these bursts differ in their occurrence, location, propagation speed,
382 amplitude, and extent. Further, post-movement bursts are characterised by higher
383 amplitude, larger extent and are slower propagation speed, suggesting distinct physiological
384 markers and functional roles pre- and post-movement. However, the comparable spectral
385 and spatial centres as well as the propagation direction of pre- and post-movement bursts
386 indicate the same underlying burst generator. Collectively, our data provide novel evidence
387 that a substantial proportion of human sensorimotor beta burst activity travels along two
388 anatomical and functional distinct axes, with distinct burst properties pre and post
389 movement.

390

391 **Distinct anatomical propagation axes of sensorimotor beta activity**

392 Traveling wave activity occurs at multiple spatial scales, ranging from mesoscopic, columnar
393 to macroscopic, transcortical levels (Muller et al., 2018). Here we show that beta burst activity
394 in human sensorimotor cortex propagates along two approximately orthogonal axes that are
395 oriented in anterior-posterior and medial-lateral direction. Recordings from invasive multi-
396 electrode arrays confirm the dominance of these two propagation axes, albeit on a smaller
397 spatial scale of roughly 4mm. For example, Takahashi and colleagues reported that beta
398 activity in M1 of a tetraplegic patient propagated along the medial-lateral axis (Takahashi et
399 al., 2011). In non-human primates, beta activity propagates along the anterior-posterior axis
400 in M1 (Balasubramanian et al., 2020; Best et al., 2016; Rubino et al., 2006; Takahashi et al.,
401 2011, 2015), and along the medial-lateral axis in the dorsal premotor cortex (Rubino et al.,
402 2006), indicating regional differences in spatiotemporal patterns (Rubino et al., 2006; Rule et
403 al., 2018).

404 In these studies, neural activity has been recorded from a single cortical region, limited by the
405 dimension of the electrode array (roughly 0.16 cm^2). By contrast, we here identified
406 spatiotemporal patterns of beta activity in burst events of an average apparent spatial width
407 of $\sim 6 \text{ cm}^2$ located in M1 and adjacent cortical areas. By leveraging high SNR MEG recordings
408 that permit high sensitivity in all signal domains, we were able to quantify bursts and their
409 spatiotemporal pattern non-invasively over these functionally cogent brain regions at a
410 spatial scale that sits between invasive recordings in animals and previous human M/EEG or
411 intracranial recordings (Alexander et al., 2016; Roberts et al., 2019; Rule et al., 2018; Stolk et
412 al., 2019; Takahashi et al., 2011). Our results extend previous invasive recordings by showing
413 that bursts activity can travel across sensory and motor cortices and bridge across functionally
414 distinct brain areas.

415
416 The spatial profiles of propagation of beta activity along the anterior-posterior and medial-
417 lateral direction are in line with the idea that propagation directions are imposed by the
418 dominant internal connections within anatomical networks (Rubino et al., 2006). Here, our
419 dominant propagation axes conformed to an anterior-posterior network comprising dorsal
420 premotor cortex, primary motor cortex and primary sensory cortex (Cauller et al., 1998;
421 Kurata, 1991; Luppino & Rizzolatti, 2000; Muakkassa & Strick, 1979) and a medial-lateral
422 network spanning across medial and lateral dorsal premotor cortex, supplementary motor
423 area cortex and caudal portions of ventral premotor cortex (Dum, 2005; Ghosh & Gattera,
424 1995; Luppino et al., 1993). The latter is thought to mirror proximal and distal sites within the
425 motor cortex (Rubino et al., 2006), with proximal representations (i.e., shoulder and elbow)
426 located more medially and distal representations (i.e., wrist and fingers) located more
427 laterally (Penfield & Boldrey, 1937). This suggests that at a macro-scale level, the direction of
428 wave propagation is dictated by the underlying horizontal connections, though further work
429 across different spatial scales (such as (Sreekumar et al., 2020)) is required to fully unpack the
430 precise relationship between sustained rhythmic synchronous spiking activity within neural
431 populations, mesoscopic and macroscopic traveling wave activity.

432
433 While our results further corroborate the importance of anterior-posterior and medial-lateral
434 propagation axes, the precise mechanism of travelling wave activity remains unclear. One
435 possible mechanism is that excitation from a single generator propagates through a network,

436 guided by conduction delays within corticocortical and the corticothalamic system
437 (Ermentrout GB, 2001; Muller et al., 2018; Preetl et al., 2000). Alternatively, travelling wave
438 activity could arise from one generator driving a network through increasing time delay, so-
439 called fictive traveling waves, or coupled generators that exhibit stable phase differences.
440 Different levels of network interactions may thus generate and sustain propagating waves.
441 Common to all travelling wave activity is the idea that they generate a consistent
442 spatiotemporal frame for further neuronal interactions. In mesoscopic data it is very
443 challenging to analytically resolve any ambiguity about the mechanism of wave generation.
444 LFP recordings with implanted electrode arrays in non-human primates suggest that coupled
445 oscillators contribute significantly to beta travelling waves over a spatial scale of 0.16cm^2
446 (Rule et al., 2018).

447

448 **Propagation axes of sensorimotor beta activity are physiologically distinct**

449 While previous work has investigated individual aspects of neural activity in relation to
450 propagation direction (Balasubramanian et al., 2020; Bhattacharya et al., 2022) we here
451 consider all signal domains of neural activity. We found that the two propagation axes can be
452 distinguished based on their physiological properties, such as propagation speed, burst
453 occurrence, amplitude, and extent. Specifically, beta activity propagating in the medial-lateral
454 direction is characterised by higher burst amplitude and larger burst extent, i.e., bursts are
455 larger in all signal domains. Further, more bursts propagate along the anterior-posterior I
456 direction, which is also characterised by faster propagation speed.

457

458 Propagating wave activity can occur in a wide range of different speeds, with propagation
459 speeds broadly falling into two categories. Speeds for mesoscopic traveling waves occurring
460 within cortical columns and their lateral connections, as identified using local field potential
461 (LFP), multielectrode arrays or optical imaging, and range between $0.1\text{-}0.8\text{m/s}$ (Bhattacharya
462 et al., 2022; Rubino et al., 2006; Takahashi et al., 2011, 2015). These slower wave speeds are
463 consistent with axonal conduction speeds of unmyelinated horizontal fibres in the superficial
464 layers of the cortex (Girard et al., 2001).

465

466 By contrast, macroscopic traveling waves spanning across several cortical regions, and
467 commonly assessed using mass-neural signal recordings such as M/EEG or ECoG, have been

468 reported at speeds ranging from around 1-10m/s (Alexander et al., 2016; Hughes, 1995;
469 Muller et al., 2018). The relatively large variability in propagation speed of macroscopic
470 traveling waves is partly due to variability in spatial resolution with low spatial resolution
471 being susceptible to aliasing artefacts (Alexander et al., 2016; Bahramisharif et al., 2013), and
472 some uncertainty in the travelled distance. Regarding the latter, while it has been
473 recommended to study travelling waves on the cortical surface (Alexander et al., 2019;
474 Hughes, 1995) it is still unclear whether neural activity truly propagates along the brains
475 cortical surface (as quantified by geodesic distance), or, at least in part, propagate through
476 the brain volume (as quantified by Euclidian distance). Further, propagation distance can be
477 computed on the original, folded cortical surface or on the inflated surface. Our data show
478 that propagation speed derived from the folded surfaces is roughly twice as fast than the
479 propagation speed derived from the inflated surface (**Supplemental Fig. 9**), which is in line
480 with the previously reported folding factor of x2.2 (Alexander et al., 2016; Burkitt et al., 2000).
481 Notwithstanding the uncertainty this introduces in estimating propagation speeds, the range
482 of propagation speeds observed here are compatible with previous reports from human and
483 non-human primates (Hughes, 1995; Muller et al., 2018), and are compatible with axonal
484 conduction speeds of myelinated cortical white matter fibres (Swadlow & Waxman, 2012),
485 suggesting an active role for macro-scale traveling burst activity in intra-areal communication
486 and information transfer.

487

488 **Pre- and post-movement burst share the same generator expressed differently**

489 The transient bursts of beta activity in our human MEG data lasted, on average, several
490 hundred milliseconds, and span over approximately 3 Hz predominantly in the lower beta
491 frequency range. These temporal and spectral properties are broadly in line with previous
492 reports (Cagnan et al., 2019; Quinn et al., 2019; Seedat et al., 2020; Shin et al., 2017; Sporn et
493 al., 2020; Tinkhauser, Pogosyan, Little, et al., 2017), with variation in the absolute values being
494 strongly dependent on how bursts are operationalised (Zich et al., 2020). We extend these
495 previous reports on the temporal and spectral burst characteristics, by additionally
496 characterising spatial burst characteristics. Sensorimotor beta burst activity often spans over
497 several square centimetres with a distinct topographic distribution. The majority of bursts are
498 located on the posterior bank of the precentral gyrus, with a proportion of bursts that spread

499 to adjacent areas. While approaching the spatial limits of human MEG, these data indicate
500 the possibility of locating beta activity within the sensorimotor cortex.

501

502 To further elucidate the generator processes and functional roles of sensorimotor beta bursts
503 we next compared pre- and post-movement bursts with regard to both their temporal,
504 spectral and spatial burst characteristics, and their propagation properties. We confirmed
505 that post-movement, compared to pre-movement, bursts occur more frequently, and are
506 stronger (i.e., higher burst amplitude) and larger in all signal domains (i.e., larger burst
507 extent). These observations are largely in line with previous studies (Quinn et al., 2019; Seedat
508 et al., 2020; Zich et al., 2018), whereby we note that (Little et al., 2019) no difference in
509 temporal burst duration between pre- and post-movement bursts was reported. We believe
510 this discrepancy is because (Little et al., 2019) employed different thresholds for pre- and
511 post-movement bursts, whereby here the same threshold was used. Moreover, we find that
512 pre-movement bursts exhibit faster propagation speed than post-movement burst activity.
513 There is no evidence that the difference in propagation speed is mediated through differences
514 in the frequency (Alexander et al., 2016), or spatial location of bursts, as both metrics are
515 comparable for pre- and post-movement bursts. The functional relevance of this difference
516 in propagation speed merits further consideration in the future, but it indicates that parsing
517 the functional role of beta activity may require its decomposition into its physiologically
518 distinct stationary and propagating components. Finally, we show that pre- and post-
519 movement bursts propagate along the same propagation axis, which is in line with previous
520 reports, observing the same propagation axes during action (Rubino et al., 2006) and rest
521 (Takahashi et al., 2011). This provides further evidence that the propagation of burst activity
522 is constrained by the underlying connectivity.

523

524 Together, our results show that, compared to pre-movement bursts, post-movement bursts
525 are stronger and larger in all signal domains, whereby their spectral and spatial centre, as well
526 as their propagation direction, are comparable. We believe this indicates that pre- and post-
527 movement bursts, therefore, share the same generator processes, which exhibits more and
528 stronger bursts post-movement. Based on biophysical principled neural modelling,
529 corticocortical and thalamocortical circuit mechanisms are thought to play a critical role in
530 generating sensorimotor beta bursts (Bonaiuto et al., 2021; Neymotin et al., 2020; Law et al.,

531 2022). Interestingly, sensorimotor beta bursts have not only been observed during action but
532 also during rest (Zich et al., 2018; Seedat et al., 2020; Becker et al., 2020; Echeverria-Altuna
533 et al., 2021), which raises the question of their functional role. That sensorimotor beta bursts
534 occur across functional states, spatial scales and species suggests that the functional role of
535 the mere presence of bursts is a very elementary one, such as maintaining the ‘status-quo’
536 (Engel & Fries, 2010) or ‘null space’ (Kaufman et al., 2014). In addition, we believe that specific
537 functional roles can be linked to the manifestation of bursts quantifiable by their temporal,
538 spectral and spatial bursts characteristics as well as their propagation properties. To give one
539 example, motor symptoms in Parkinson’s disease have been linked to prolonged burst
540 duration (Deffains et al., 2018; Tinkhauser, Pogosyan, Little, et al., 2017; Tinkhauser,
541 Pogosyan, Tan, et al., 2017). The proposed hierarchical dual-role framework of burst function
542 can be tested using biophysical models (Neymotin et al., 2020) and targeted neuromodulatory
543 experiments.

544

545 **Caveats of spatial and spatiotemporal properties in source space**

546 Non-invasive techniques have limitations that should be considered when interpreting the
547 spatial domain of bursts and travelling wave activity. LCMV beamformers assume that each
548 source is a single dipole and that there are no other correlated sources in the brain. These
549 limitations make interpretation of spatial structure in LCMV power maps ambiguous. We
550 explore several specific issues: firstly, whether the apparent spatial extent of a source is
551 simply modulated by the SNR of the signal. Secondly, the inherent smoothness of the source
552 reconstruction maps due to the mapping of a few hundred sensors to several thousand voxels.
553 Finally, if a patch of cortex is active rather than a single point-source, then these correlated
554 voxels can suppress the signal of interest. Each of these points can be challenging when
555 interpreting the spatial domain of bursts and travelling waves.

556

557 The first issue suggests that differences in the bursts’ apparent spatial width could simply be
558 caused by differences in SNR across and/or within sessions rather than differences in the
559 spatial distribution of cortical activity. We performed one beamformer per session, thus
560 different SNR levels across sessions would affect the beamformer weights. However, if
561 variation across sessions in beamformer weights would explain variation in bursts’ apparent
562 spatial width, we would expect a negative relationship between burst amplitude and burst

563 apparent spatial width across sessions. This is not the case in our data, suggesting that
564 between-session differences in beamformer weights do not cause the observed differences
565 in bursts' apparent spatial width. Nevertheless, spatial width of burst activity measured with
566 M/EEG or ECoG should be interpreted with caution. Here, due to the strong correlation
567 between the bursts' apparent spatial width, temporal duration, and frequency spread, we
568 combined these signal properties using PCA and used the resulting cross-modal measure
569 burst extent.

570

571 Secondly, the inherent smoothness of the beamformer solution can lead to 'trivial' structure
572 in the source solution, meaning that single sources can leak across cortex or that multiple
573 sources can become blurred together. Across space in bursts diverse phase lags exists
574 suggesting that structure is unlikely to have arisen solely from leakage of a single source. The
575 functional role of travelling waves remains unclear. As outlined above, the mechanisms
576 underlying travelling waves remain ambiguous (see discussion section: **Distinct anatomical**
577 **propagation axes of sensorimotor beta activity**), both at the meso- and macro scale (Hughes,
578 1995; Muller et al., 2018). We cannot rule out the possibility that this phase structure arises
579 from mixing of multiple distinct sources but take a 'gradient' or 'travelling wave' perspective
580 here to better link with comparative literature. While this concerns travelling wave analyses
581 across a range of spatial scales and recording techniques; source space analysis, as employed
582 here, entails an additional issue – namely whether the propagation directions can be trivially
583 explained by spatial variability in the beamformer weights. Our control analysis showed that
584 the estimated propagation direction correlates significantly with the propagation direction
585 obtained after regressing out the main components of spatial variability in the beamformer
586 weights. This indicates that beamformer weights can contribute to, but do not solely explain
587 spatiotemporal gradients in human MEG data.

588 Finally, patches of high amplitude, correlated sources can be mutually suppressed by the
589 LCMV beamformer leading to an apparent loss of signal. Though we cannot remove the
590 possibility these mutual correlations may be suppressing part of the signal, we observe strong
591 task-related activity suggesting that a substantial proportion remains in our analysis.

592

593 Together, we acknowledge that the beamformer weights can affect bursts' spatial width and
594 propagation direction but believe that our control analyses suggests that the beamformer
595 weights are not driving the observed effects.

596

597 **Materials ad Methods**

598 **Participants and experimental task**

599 The study was approved by the UCL Research Ethics Committee (reference number 5833/001)
600 and conducted in accordance with the Declaration of Helsinki. Informed written consent was
601 obtained from all participants. All participants (6 male, $M = 28.5$ years, $SD = 8.52$ years across
602 individuals) were free of neurological or psychiatric disorders, right-handed and had normal
603 or corrected-to-normal vision.

604 Participants performed a visually cued action decision making task in which they responded
605 to visual stimuli projected onto a screen by pressing one of two buttons using their right index
606 or middle finger (for details see (Bonaiuto et al., 2018)). The task uses a factorial design with
607 congruence (congruent, incongruent) and coherence (low, medium, high). Here we only
608 consider congruent, high coherence trials (42 trials per block) that were responded to
609 correctly (for full design see (Bonaiuto et al., 2018; Little et al., 2019)).

610

611 **MRI acquisition and processing**

612 Prior to the MEG sessions, structural MRI data were acquired using a 3T Magnetom TIM Trio
613 MRI scanner (Siemens Healthcare, Erlangen, Germany). A T1-weighted 3D spoiled fast low
614 angle shot (FLASH) sequence was acquired to generate an accurate image of the scalp for
615 head-cast construction. Subject-specific head-casts optimise co-registration and reduce head
616 movements, and thereby significantly improve the signal to noise ratio. See (Bonaiuto et al.,
617 2018; Meyer et al., 2017; Troebinger et al., 2014) for details on the sequence and the head-
618 cast construction.

619 In addition, a high-resolution, quantitative, multiple parameter mapping (MPM) protocol,
620 consisting of 3 differentially-weighted, RF and gradient spoiled, multi-echo 3D FLASH
621 acquisitions recorded with whole-brain coverage at 800 mm isotropic resolution, was
622 performed. See (Bonaiuto et al., 2018) for details on the protocol. Each quantitative map was
623 co-registered to the scan used to design the head-cast, using the T1 weighted map. Individual
624 cortical surface meshes were extracted using FreeSurfer (v5.3.0; (Fischl, 2012)) from
625 multiparameter maps using the PD and T1 sequences as inputs, with custom modifications to
626 avoid tissue boundary segmentation failures (Carey et al., 2018). Meshes were down-sampled
627 by a factor of 10 (vertices: $M = 30,095$, $SD = 2,665$ across individuals; faces: $M = 60,182$, $SD =$

628 5,331 across individuals) and smoothed (5mm). Here we used the original and the inflated
629 pial surface.

630

631 **MEG acquisition and pre-processing**

632 MEG data were acquired using a 275-channel Canadian Thin Films (CTF) MEG system using
633 individual head-casts in a magnetically shielded room. Head position was localised using three
634 fiducial coils placed at the nasion and left/right pre-auricular points, within the head-cast.
635 Data were sampled at 1200Hz. A projector displayed the visual stimuli on a screen (~50 cm
636 from the participant), and participants made responses with a button box.

637

638 A summary of the data processing pipeline is shown in **Supplemental Fig. 1**. MEG data were
639 analysed using the OHBA Software Library (OSL: [https://ohba-
640 analysis.github.io/osl-
641 docs/](https://ohba-analysis.github.io/osl-docs/)). MEG data were processed in for each block separately unless stated otherwise. Firstly, raw
642 data were converted to SPM12 format for analysis in Matlab2019b. Registration between
643 structural MRI and the MEG data was performed with RHINO (Registration of head shapes
644 Including Nose in OSL) using only the Fiducial landmarks and single shell as forward model.
645 Unless stated otherwise data were analysed in single subject space.

646 Continuous data were down-sampled to 300Hz. Further, a band-pass (1-95Hz) and notch-filter
647 (49-51Hz) were applied. Time segments containing artefacts were identified by using
648 generalised extreme studentized deviate method (GESD (Rosner, 1983)) on the standard
649 deviation of the signal across all sensors in 1s non-overlapping windows, with a maximum
650 number of outliers limited to 20% of the data and adopting a significance level of 0.05. Data
651 segments identified as outliers were excluded from subsequent analyses.

652 Further, denoising was applied using independent component analysis (ICA) using temporal
653 FastICA across sensors (Hyvarinen, 1999). 62 independent components were estimated and
654 components representing stereotypical artefacts such as eye blinks, eye movements, and
655 electrical heartbeat activity were manually identified and regressed out of the data.

656 Data were then filtered to the frequency band of interest (β 13-30 Hz) and segmented from -
657 2s to 2s relative to the button press. Segmented data were projected onto subjects' individual
658 cortical surface meshes using a Linearly Constrained Minimum Variance (LCMV) vector
659 beamformer (Van Veen & Buckley, 1988; Woolrich et al., 2011). The beamformer weights
660 were estimated at the centre of each face, referred to henceforth as spatial locations. A

660 covariance matrix was computed across all segments and was regularised to 55 dimensions
661 using principal component analysis (PCA). All analyses are conducted in source space.

662

663 **Time-frequency decomposition**

664 Time-frequency analysis was applied to single trials and spatial locations using dpss-based
665 multitaper (window = 1.6s, steps = 200ms) with a frequency resolution of 1Hz. Epochs were
666 baseline corrected (-1.8s to -1.1s). This procedure results in a trial-by-trial time-frequency
667 decomposition for each spatial location, i.e., relative power in 4D, time x frequency x space x
668 trial, whereby space is on its own 3-dimensional (x, y, z coordinates of surface locations).

669

670 **Burst operationalisation**

671 We used binarization and high-dimensional clustering to operationalize beta bursts. Power
672 derived from time-frequency analysis was first binarized using a simple amplitude threshold
673 (see **Supplemental Methods**). The threshold was obtained empirically, as in previous work
674 (Little et al., 2019). Specifically, trial-wise power was correlated with the burst probability
675 across a range of different threshold values (median to median plus seven standard
676 deviations, in steps of 0.25). The threshold value that retained the highest correlation
677 between trial-wise power and burst probability was used to binarize the data. To account for
678 difference in signal-to-noise across sessions, days and subjects we obtained one threshold per
679 session ($M = 2.97 \times SDs$ above mean, $SD = 0.66$ across sessions; **Supplemental Fig. 2**).

680 Following binarization, data were clustered across time, frequency, and space on a single trial
681 level (see **Supplemental Methods**). Burst identification was limited to the time of interest (-2
682 to 2s relative to the button press), the frequency of interest (13-30Hz) and region of interest
683 (ROI, left-hand area). To restrict the burst analysis to a ROI, volume-based ROIs in MNI space
684 were normalised to subject's native space using the inverse deformation field and
685 transformed to surface-based ROIs. Clusters had to span at least 2 time points, frequency
686 steps and spatial locations to be considered further.

687

688 **Burst characteristics**

689 We divide burst characteristics into 1st and 2nd level burst characteristics. We define 1st level
690 burst characteristics as characteristics that are obtained for each burst and each domain
691 separately. **Fig. 1** illustrates the first level characteristics. For the temporal domain, burst

692 temporal on- and offset, temporal duration and centre (i.e., mean of on- and offset) were
693 obtained. Equally, low and high frequency boundaries, frequency spread and centre (i.e.,
694 mean of low and high boundary) were extracted for the spectral domain. For the spatial
695 domain we obtained the spatial width (i.e., total surface area defined as the sum of the area
696 of all faces), the size in each dimension (x, y, z) using the minimum bounding rectangle (i.e.,
697 bounding box), and the spatial centre. The spatial centre is defined as the projection of the
698 centre of mass onto the surface. The spatial centre can be described using its Cartesian
699 coordinates. An alternative to the description of the spatial centre is provided by the first two
700 components of a PCA of the Cartesian coordinates (**Supplemental Fig. 7**). The first two PCs
701 describing 98% of variance are retained for further analysis. The first PC (76.3% variance
702 explained) contains a spatial gradient along the anterior/lateral – posterior/medial axis. The
703 second PC (22.3% variance explained) contains a spatial gradient along the anterior/medial –
704 posterior/lateral axis. Thus, the location of an individual burst can be described by the two PC
705 scores, relating to the amount of each PC that it contains. In addition, burst amplitude was
706 obtained, i.e., the mean amplitude across all time points, frequencies, and spatial locations of
707 the burst.

708 These 1st level burst characteristics form the basis for 2nd level burst characteristics. These can
709 be broadly summarised as a) combinations and b) interactions of characteristics within and
710 across domains. Here we extract one of these measures: temporal duration, frequency
711 spread, and apparent spatial width were combined to a single metric, i.e., burst extend. The
712 three measures are highly correlated within subjects ($M = 0.785$; $SD = 0.021$, across the three
713 correlations and eight individuals, **Supplemental Fig. 10a,b**) and where therefore reduced to
714 a single metric using PCA. The first principal component explains 85.6% of the variance and is
715 defined as burst extent (PC 2: 7.5%, PC 3: 6.9%, **Supplemental Fig. 10c**).

716

717 **Propagation direction and speed of neural activity within bursts**

718 To investigate whether activity within human sensorimotor bursts propagates, we identified
719 the dominant propagation direction and speed for each burst. To this end, data (before time-
720 frequency decomposition, see **Supplemental Fig. 1**) of each burst were extracted from burst
721 on- to offset for each surface location in the burst. The sign ambiguity in the beamforming
722 process entails that the spatial locations within a burst may have arbitrarily opposite signs.
723 This is not an issue when estimating power, as above, but can impact on the estimation of the

724 propagation direction. Sign ambiguity was resolved using the sign-flipping algorithm
725 described in (Vidaurre et al., 2018). For a finer temporal resolution data were interpolated by
726 a factor of 10.

727 For each burst, we estimated the propagation direction and propagation speed. Propagation
728 direction and speed were estimated from critical points in the oscillatory cycle (four critical
729 points per oscillatory cycle, i.e., peak and trough as well as peak-trough and trough-peak
730 midpoint, grey vertical lines in **Fig. 2a**) and then averaged across critical points within one
731 burst.

732 The propagation direction at each critical point was estimated from the relative latency (i.e.,
733 absolute latency of that critical point at each surface location relative to absolute latency of
734 that critical point for the average across all surface locations in that burst). For example, **Fig.**
735 **2b_i** shows the relative latency for each surface location in the burst for the critical point at
736 212ms in the burst. Next, from these relative latencies and their surface locations the
737 propagation direction was estimated. Specifically, propagation direction was estimated using
738 linear regression (Balasubramanian et al., 2020), whereby the relative latency at the surface
739 location was predicted from the coordinates of the surface location of the inflated surface.
740 On the inflated surface, a gradient in the z-direction is always depicted by a gradient in x- or
741 y-direction, which is why only two simple linear regressions were estimated, one for the x-
742 and one for the y-direction (**Fig. 2b_{ii}**). Propagation direction along the x-y-direction was
743 obtained by transforming the regression coefficients from Cartesian coordinates to spherical
744 coordinates (red arrow in **Fig. 2b_{iii}**). For each regression, its associated coefficient of
745 determination (R^2) was calculated and the two R^2 's averaged. This approach results in one
746 propagation direction and one R^2 per critical point.

747 Propagation direction across critical points was obtained by clustering (i.e., Spectral
748 clustering) the propagation directions across critical points. Three scenarios existed: 1) One
749 cluster was obtained and the variance across directions of critical points was relatively low
750 (standard deviation $< \pi/4$; **Fig. 2b_{iii}**; **Supplemental Fig. 5a**); 2) One cluster was obtained and
751 the variance across directions of critical points was relatively high (standard deviation $> \pi/4$;
752 **Supplemental Fig. 5b**); 3) More than one cluster was obtained (**Supplemental Fig. 5c**).
753 Scenario 2 and scenario 3 indicate complex propagation patterns, such as random or circular
754 patterns (Denker et al., 2018; Rule et al., 2018). Based on previous literature we expect planar
755 traveling waves to be dominant in the primary motor cortex (Balasubramanian et al., 2020;

756 Rubino et al., 2006; Rule et al., 2018; Takahashi et al., 2011). For bursts of scenario 1
757 propagation directions and R^2 were averaged across critical points (back arrow in **Fig. 2b**_{iii}).
758 To have sufficient confidence in the direction bursts with an average $R^2 < 0.2$ were discarded
759 (Balasubramanian et al., 2020). Following this procedure, we found that 79.59% ($SD = 2.37\%$
760 across individuals) of the bursts show a spatiotemporal pattern ($R^2: M = 0.35, SD = 0.02$ across
761 individuals). To combine propagation directions across subjects, propagation directions were
762 spatially normalised to MNI space using the deformation field. Directions are presented as
763 probability distributions. On the average of the probability distributions across subjects the
764 propagation direction was quantified using a mixture of von Mises functions.
765 The propagation speed at each critical point was defined as the distance between the spatial
766 locations with the largest and smallest relative latency divided by the difference in their
767 latencies (Bahramisharif et al., 2013). Distance was computed using exact geodesic distance
768 (**Fig. 2c**_{ii}) on the inflated surface. See **Supplemental Methods** and **Supplemental Fig. 9** for a
769 comparison of propagation speed when computing the distance on the inflated surface and
770 the original surface. Propagation speed was averaged across critical points.

771

772 **Accuracy of the propagation direction detection in simulated and real meshes**

773 Using simulation, we evaluated the accuracy of the propagation direction estimation. To this
774 end, we generated 360 noise-free high-resolution gradients span 1deg in steps of 1deg (**Fig.**
775 **3a** shows a subset). To evaluate the effect of mesh type and spatial sampling we created three
776 2D mesh types, 1) square mesh (**Fig. 3b**), 2) circular mesh (**Fig. 3c**), and 3) random mesh (**Fig.**
777 **3d**), whereby each mesh type was sampled at three spatial sampling rates: $N/2$, N , and $N \times 2$
778 (N approximates the spatial sampling of the surface mesh, i.e., roughly 27 surface locations
779 per cm^2). For each gradient and each mesh, the propagation direction was estimated and the
780 estimation error, i.e., difference between true and estimated propagation direction,
781 computed. For the random mesh, this procedure was repeated 100 times, each time with a
782 different random mesh.

783 As the surface mesh is irregular and each burst is unique in its spatial size and shape, we
784 additionally evaluated the accuracy of the propagation direction estimation for the real
785 bursts. To this end, for each individual burst and each gradient, the propagation direction was
786 estimated, and the estimation error computed as above.

787

788 **Control analysis**

789 The ill-posed nature of the inverse problem in M/EEG means that the source estimation has
790 a degree of smoothness. While this is unavoidable and shared with all inverse problem
791 methods, the smoothness can be problematic when interpreting the spatial domain of burst
792 and their spatiotemporal gradients, travelling waves. We perform a series of control analysis
793 to explore the practical effect of these ambiguities in our data. Our reasoning was that with
794 regards to interpreting the spatial width of burst activity, any differences could be caused by
795 differences in SNR across and/or within sessions rather than differences in the spatial
796 distribution of cortical activity (see **Supplemental Fig. 4ai, bi** for a schematic illustration). To
797 address this, we performed several correlation analyses between burst amplitude and burst
798 apparent spatial width, between and across sessions.

799 Regarding the interpretation of traveling waves, there is inherent ambiguity concerning the
800 mechanisms that generate a travelling wave (see discussion section: **Distinct anatomical**
801 **propagation axes of sensorimotor beta activity**; Prechtl et al., 2000; Ermentrout and
802 Kleinfeld 2001). While this concerns travelling wave analyses across a range of spatial scales
803 and recording techniques, the source space analysis employed here entails an additional issue
804 – namely whether the propagation directions can be trivially explained by spatial variability
805 in the LCMV weights. To address this issue, we correlated the latency of the critical points
806 across space before and after regressing out the main components of the spatial variability in
807 the LCMV weights. Specifically, we performed PCA on the LCMV weights and retained the
808 components that explained 90% of the variance in the LCMV weights. We then performed,
809 for each critical point of each burst, a multiple regression analysis with the latencies of the
810 critical point across space as dependent variable and the coefficients of the PCs across space
811 as independent variables. We then correlated the latency of the critical points across space
812 with the residuals of the multiple regression. Pearson's r was first averaged across critical
813 points within bursts, and then across bursts.

814

815 **Statistical analysis**

816 Statistical analysis was performed using nonparametric testing in Matlab2019b. If not stated
817 otherwise, descriptive statistics depict mean and standard deviation of the median across
818 subjects. Burst characteristics with unimodal distributions (e.g., burst amplitude, burst
819 propagation speed), were compared using Wilcoxon signed-rank test on the medians of the

820 distribution. The test statistic is reported as a value of T . Burst characteristics with multimodal
821 distributions (e.g., spatial location) were compared using two-sample Kolmogorov–Smirnov
822 test on the single subject level. Test statistic is reported as value of KS (i.e., mean and range
823 across subjects). Two circular distributions (e.g., propagation direction pre- and post-
824 movement) were compared using two-sample Watson’s U^2 test (Landler et al., 2021) on the
825 single subject level. Test statistic is reported as value of U^2 test (i.e., mean and range across
826 subjects).

827 To test whether there is significant spatiotemporal structure in burst activity, we compared
828 the propagation direction of real and surrogate data. Specifically, for a subset of bursts, i.e.,
829 100 randomly selected bursts, 1000 surrogates were created for each burst from the data
830 after sign ambiguity was resolved (see **Supplemental Fig. 1**). Surrogate data were obtained
831 by computing the discrete Fourier transform of the data, randomizing the phase spectrum
832 while preserving the amplitude spectrum, and then computing the inverse discrete Fourier
833 transform to obtain the surrogated data (method 3 in (Hurtado et al., 2004)). For each burst,
834 the magnitude of the propagation direction of the real data was compared to the distribution
835 from 1000 surrogates.

836 To quantify the overall propagation direction, a mixture of four von Mises functions was fitted
837 to the average of the subjects’ probability distribution of propagation directions across bursts.
838 This provides an estimate of the angle and length of the von Mises functions. Reliability of
839 von Mises functions was assessed using a split-half reliability. 500 split halves were computed
840 and four von Mises functions estimated on each half independently. For both, angle and
841 length, the difference between the two halves was computed. Further, to test whether the
842 von Mises functions were significantly different from zero, non-parametric permutation
843 testing was employed on the length of the von Mises functions. Permutations were carried
844 out by randomising the propagation direction of each burst. 5000 permutations were
845 computed before statistical significance was determined on the length of the von Mises
846 functions while correcting for multiple comparison at $p < 0.01$.

847

848 **Acknowledgements**

849 C.Z. is supported by the Brain Research UK (201718-13, 201617-03). A.J.Q. is supported by the
850 NIHR Oxford Health Biomedical Research Centre and a Wellcome Trust Strategic Award
851 (098369/Z/12/Z). G.C.O. is supported by EPSRC (EP/T001046/1) funding from the Quantum

852 Technology hub in sensing and timing (sub-award QTPRF02). L.C.M. is supported by the
853 Medical Research Council (MR/N013867/1). The Wellcome Centre for Human Neuroimaging
854 and The Wellcome Centre for Integrative Neuroimaging are supported by core funding from
855 the Wellcome Trust (203147/Z/16/Z and 203139/Z/16/Z, respectively).

856 **References**

- 857 Alexander, D. M., Ball, T., Schulze-Bonhage, A., & van Leeuwen, C. (2019). Large-scale
858 cortical travelling waves predict localized future cortical signals. *PLOS Computational*
859 *Biology*, 15(11), e1007316. <https://doi.org/10.1371/journal.pcbi.1007316>
- 860 Alexander, D. M., Nikolaev, A. R., Jurica, P., Zvyagintsev, M., Mathiak, K., & van Leeuwen, C.
861 (2016). Global Neuromagnetic Cortical Fields Have Non-Zero Velocity. *PLOS ONE*,
862 11(3), e0148413. <https://doi.org/10.1371/journal.pone.0148413>
- 863 Bahramisharif, A., van Gerven, M. A. J., Aarnoutse, E. J., Mercier, M. R., Schwartz, T. H.,
864 Foxe, J. J., Ramsey, N. F., & Jensen, O. (2013). Propagating Neocortical Gamma Bursts
865 Are Coordinated by Traveling Alpha Waves. *Journal of Neuroscience*, 33(48), 18849–
866 18854. <https://doi.org/10.1523/JNEUROSCI.2455-13.2013>
- 867 Balasubramanian, K., Papadourakis, V., Liang, W., Takahashi, K., Best, M. D., Suminski, A. J.,
868 & Hatsopoulos, N. G. (2020). Propagating Motor Cortical Dynamics Facilitate
869 Movement Initiation. *Neuron*, 106(3), 526-536.e4.
870 <https://doi.org/10.1016/j.neuron.2020.02.011>
- 871 Best, M. D., Suminski, A. J., Takahashi, K., Brown, K. A., & Hatsopoulos, N. G. (2016). Spatio-
872 Temporal Patterning in Primary Motor Cortex at Movement Onset. *Cerebral Cortex*,
873 27(2). <https://doi.org/10.1093/cercor/bhv327>
- 874 Bhattacharya, S., Brincat, S. L., Lundqvist, M., & Miller, E. K. (2022). Traveling waves in the
875 prefrontal cortex during working memory. *PLOS Computational Biology*, 18(1),
876 e1009827. <https://doi.org/10.1371/journal.pcbi.1009827>
- 877 Bonaiuto, J. J., Little, S., Neymotin, S. A., Jones, S. R., Barnes, G. R., & Bestmann, S. (2021).
878 Laminar dynamics of high amplitude beta bursts in human motor cortex.
879 *NeuroImage*, 242, 118479. <https://doi.org/10.1016/j.neuroimage.2021.118479>

- 880 Bonaiuto, J. J., Meyer, S. S., Little, S., Rossiter, H., Callaghan, M. F., Dick, F., Barnes, G. R., &
881 Bestmann, S. (2018). Lamina-specific cortical dynamics in human visual and
882 sensorimotor cortices. *ELife*, 7, e33977. <https://doi.org/10.7554/eLife.33977>
- 883 Brittain, J.-S., & Brown, P. (2014). Oscillations and the basal ganglia: Motor control and
884 beyond. *NeuroImage*, 85, 637–647.
885 <https://doi.org/10.1016/j.neuroimage.2013.05.084>
- 886 Burkitt, G. R., Silberstein, R. B., Cadusch, P. J., & Wood, A. W. (2000). Steady-state visual
887 evoked potentials and travelling waves. *Clinical Neurophysiology*, 111(2), 246–258.
888 [https://doi.org/10.1016/S1388-2457\(99\)00194-7](https://doi.org/10.1016/S1388-2457(99)00194-7)
- 889 Cagnan, H., Mallet, N., Moll, C. K. E., Gulberti, A., Holt, A. B., Westphal, M., Gerloff, C., Engel,
890 A. K., Hamel, W., Magill, P. J., Brown, P., & Sharott, A. (2019). Temporal evolution of
891 beta bursts in the parkinsonian cortical and basal ganglia network. *Proceedings of*
892 *the National Academy of Sciences*, 116(32), 16095–16104.
893 <https://doi.org/10.1073/pnas.1819975116>
- 894 Carey, D., Caprini, F., Allen, M., Lutti, A., Weiskopf, N., Rees, G., Callaghan, M. F., & Dick, F.
895 (2018). Quantitative MRI provides markers of intra-, inter-regional, and age-related
896 differences in young adult cortical microstructure. *NeuroImage*, 182, 429–440.
897 <https://doi.org/10.1016/j.neuroimage.2017.11.066>
- 898 Carhart-Harris, R. L. (2018). The entropic brain—Revisited. *Neuropharmacology*, 142, 167–
899 178. <https://doi.org/10.1016/j.neuropharm.2018.03.010>
- 900 Carhart-Harris, R. L., Leech, R., Hellyer, P. J., Shanahan, M., Feilding, A., Tagliazucchi, E.,
901 Chialvo, D. R., & Nutt, D. (2014). The entropic brain: A theory of conscious states
902 informed by neuroimaging research with psychedelic drugs. *Frontiers in Human*
903 *Neuroscience*, 8. <https://doi.org/10.3389/fnhum.2014.00020>

- 904 Cauller, L. J., Clancy, B., & Connors, B. W. (1998). Backward cortical projections to primary
905 somatosensory cortex in rats extend long horizontal axons in layer I. *The Journal of*
906 *Comparative Neurology*, 390(2), 297–310. [https://doi.org/10.1002/\(SICI\)1096-](https://doi.org/10.1002/(SICI)1096-)
907 9861(19980112)390:2<297::AID-CNE11>3.0.CO;2-V
- 908 Davis, Z. W., Benigno, G. B., Fletteman, C., Desbordes, T., Steward, C., Sejnowski, T. J., H.
909 Reynolds, J., & Muller, L. (2021). Spontaneous traveling waves naturally emerge from
910 horizontal fiber time delays and travel through locally asynchronous-irregular states.
911 *Nature Communications*, 12(1), 6057. <https://doi.org/10.1038/s41467-021-26175-1>
- 912 Davis, Z. W., Muller, L., Martinez-Trujillo, J., Sejnowski, T., & Reynolds, J. H. (2020).
913 Spontaneous travelling cortical waves gate perception in behaving primates. *Nature*,
914 587(7834), 432–436. <https://doi.org/10.1038/s41586-020-2802-y>
- 915 Deffains, M., Iskhakova, L., Katabi, S., Israel, Z., & Bergman, H. (2018). Longer β oscillatory
916 episodes reliably identify pathological subthalamic activity in Parkinsonism: Longer
917 STN β Episodes Are a PD Biomarker. *Movement Disorders*, 33(10), 1609–1618.
918 <https://doi.org/10.1002/mds.27418>
- 919 Denker, M., Zehl, L., Kilavik, B. E., Diesmann, M., Brochier, T., Riehle, A., & Grün, S. (2018).
920 LFP beta amplitude is linked to mesoscopic spatio-temporal phase patterns. *Scientific*
921 *Reports*, 8(1), 5200. <https://doi.org/10.1038/s41598-018-22990-7>
- 922 Ding, Y., & Ermentrout, B. (2021). Traveling waves in non-local pulse-coupled networks.
923 *Journal of Mathematical Biology*, 82(3), 18. <https://doi.org/10.1007/s00285-021->
924 01572-8
- 925 Dum, R. P. (2005). Frontal Lobe Inputs to the Digit Representations of the Motor Areas on
926 the Lateral Surface of the Hemisphere. *Journal of Neuroscience*, 25(6), 1375–1386.
927 <https://doi.org/10.1523/JNEUROSCI.3902-04.2005>

- 928 Engel, A. K., & Fries, P. (2010). Beta-band oscillations—Signalling the status quo? *Current*
929 *Opinion in Neurobiology*, 20(2), 156–165.
930 <https://doi.org/10.1016/j.conb.2010.02.015>
- 931 Enz, N., Ruddy, K. L., Rueda-Delgado, L. M., & Whelan, R. (2021). Volume of β -Bursts, But
932 Not Their Rate, Predicts Successful Response Inhibition. *The Journal of Neuroscience*,
933 41(23), 5069–5079. <https://doi.org/10.1523/JNEUROSCI.2231-20.2021>
- 934 Ermentrout GB, K. (2001). *Traveling Electrical Waves in Cortex: Insights from Phase*
935 *Dynamics and Speculation on a Computational Role*. 29, 33–44.
- 936 Feingold, J., Gibson, D. J., DePasquale, B., & Graybiel, A. M. (2015). Bursts of beta oscillation
937 differentiate postperformance activity in the striatum and motor cortex of monkeys
938 performing movement tasks. *Proceedings of the National Academy of Sciences*,
939 112(44), 13687–13692. <https://doi.org/10.1073/pnas.1517629112>
- 940 Fischl, B. (2012). FreeSurfer. *NeuroImage*, 62(2), 774–781.
941 <https://doi.org/10.1016/j.neuroimage.2012.01.021>
- 942 Ghosh, S., & Gattera, R. (1995). A Comparison of the Ipsilateral Cortical Projections to the
943 Dorsal and Ventral Subdivisions of the Macaque Premotor Cortex. *Somatosensory &*
944 *Motor Research*, 12(3–4), 359–378. <https://doi.org/10.3109/08990229509093668>
- 945 Gilbertson, T., Lalo, E., Doyle, L., Di Lazzaro, V., Cioni, B., & Brown, P. (2005). Existing motor
946 state is favored at the expense of new movement during 13-35 Hz oscillatory
947 synchrony in the human corticospinal system. *The Journal of Neuroscience: The*
948 *Official Journal of the Society for Neuroscience*, 25(34), 7771–7779.
949 <https://doi.org/10.1523/JNEUROSCI.1762-05.2005>

- 950 Girard, P., Hupé, J. M., & Bullier, J. (2001). Feedforward and feedback connections between
951 areas V1 and V2 of the monkey have similar rapid conduction velocities. *Journal of*
952 *Neurophysiology*, 85(3), 1328–1331. <https://doi.org/10.1152/jn.2001.85.3.1328>
- 953 Heideman, S. G., Quinn, A. J., Woolrich, M. W., van Ede, F., & Nobre, A. C. (2020). Dissecting
954 beta-state changes during timed movement preparation in Parkinson’s disease.
955 *Progress in Neurobiology*, 184, 101731.
956 <https://doi.org/10.1016/j.pneurobio.2019.101731>
- 957 Heitmann, S., Rule, M., Truccolo, W., & Ermentrout, B. (2017). Optogenetic Stimulation
958 Shifts the Excitability of Cerebral Cortex from Type I to Type II: Oscillation Onset and
959 Wave Propagation. *PLOS Computational Biology*, 13(1), e1005349.
960 <https://doi.org/10.1371/journal.pcbi.1005349>
- 961 Hughes, J. R. (1995). The Phenomenon of Travelling Waves: A Review. *Clinical*
962 *Electroencephalography*, 26(1), 1–6. <https://doi.org/10.1177/155005949502600103>
- 963 Hurtado, J. M., Rubchinsky, L. L., & Sigvardt, K. A. (2004). Statistical Method for Detection of
964 Phase-Locking Episodes in Neural Oscillations. *Journal of Neurophysiology*, 91(4),
965 1883–1898. <https://doi.org/10.1152/jn.00853.2003>
- 966 Hyvarinen, A. (1999). Fast and robust fixed-point algorithms for independent component
967 analysis. *IEEE Transactions on Neural Networks*, 10(3), 626–634.
968 <https://doi.org/10.1109/72.761722>
- 969 Jones, S. R. (2016). When brain rhythms aren’t ‘rhythmic’: Implication for their mechanisms
970 and meaning. *Current Opinion in Neurobiology*, 40, 72–80.
971 <https://doi.org/10.1016/j.conb.2016.06.010>

- 972 Joundi, R. A., Jenkinson, N., Brittain, J.-S., Aziz, T. Z., & Brown, P. (2012). Driving Oscillatory
973 Activity in the Human Cortex Enhances Motor Performance. *Current Biology*, *22*(5),
974 403–407. <https://doi.org/10.1016/j.cub.2012.01.024>
- 975 Kaufman, M. T., Churchland, M. M., Ryu, S. I., & Shenoy, K. V. (2014). Cortical activity in the
976 null space: Permitting preparation without movement. *Nature Neuroscience*, *17*(3),
977 440–448. <https://doi.org/10.1038/nn.3643>
- 978 Khanna, P., & Carmena, J. M. (2017). Beta band oscillations in motor cortex reflect neural
979 population signals that delay movement onset. *ELife*, *6*, e24573.
980 <https://doi.org/10.7554/eLife.24573>
- 981 Kurata, K. (1991). Corticocortical inputs to the dorsal and ventral aspects of the premotor
982 cortex of macaque monkeys. *Neuroscience Research*, *12*(1), 263–280.
983 [https://doi.org/10.1016/0168-0102\(91\)90116-G](https://doi.org/10.1016/0168-0102(91)90116-G)
- 984 Landler, L., Ruxton, G. D., & Malkemper, E. P. (2021). Advice on comparing two independent
985 samples of circular data in biology. *Scientific Reports*, *11*(1), 20337.
986 <https://doi.org/10.1038/s41598-021-99299-5>
- 987 Law, R. G., Pugliese, S., Shin, H., Sliva, D. D., Lee, S., Neymotin, S., Moore, C., & Jones, S. R.
988 (2022). Thalamocortical Mechanisms Regulating the Relationship between Transient
989 Beta Events and Human Tactile Perception. *Cerebral Cortex*, *32*(4), 668–688.
990 <https://doi.org/10.1093/cercor/bhab221>
- 991 Little, S., Bonaiuto, J., Barnes, G., & Bestmann, S. (2019). Human motor cortical beta bursts
992 relate to movement planning and response errors. *PLOS Biology*, *17*(10), e3000479.
993 <https://doi.org/10.1371/journal.pbio.3000479>

- 994 Luppino, G., Matelli, M., Camarda, R., & Rizzolatti, G. (1993). Corticocortical connections of
995 area F3 (SMA-proper) and area F6 (pre-SMA) in the macaque monkey. *The Journal of*
996 *Comparative Neurology*, 338(1), 114–140. <https://doi.org/10.1002/cne.903380109>
- 997 Luppino, G., & Rizzolatti, G. (2000). The Organization of the Frontal Motor Cortex.
998 *Physiology*, 15(5), 219–224. <https://doi.org/10.1152/physiologyonline.2000.15.5.219>
- 999 Meyer, S. S., Bonaiuto, J., Lim, M., Rossiter, H., Waters, S., Bradbury, D., Bestmann, S.,
1000 Brookes, M., Callaghan, M. F., Weiskopf, N., & Barnes, G. R. (2017). Flexible head-
1001 casts for high spatial precision MEG. *Journal of Neuroscience Methods*, 276, 38–45.
1002 <https://doi.org/10.1016/j.jneumeth.2016.11.009>
- 1003 Muakkassa, K. F., & Strick, P. L. (1979). Frontal lobe inputs to primate motor cortex:
1004 Evidence for four somatotopically organized ‘premotor’ areas. *Brain Research*,
1005 177(1), 176–182. [https://doi.org/10.1016/0006-8993\(79\)90928-4](https://doi.org/10.1016/0006-8993(79)90928-4)
- 1006 Muller, L., Chavane, F., Reynolds, J., & Sejnowski, T. J. (2018). Cortical travelling waves:
1007 Mechanisms and computational principles. *Nature Reviews Neuroscience*, 19(5),
1008 255–268. <https://doi.org/10.1038/nrn.2018.20>
- 1009 Neymotin, S. A., Daniels, D. S., Caldwell, B., McDougal, R. A., Carnevale, N. T., Jas, M.,
1010 Moore, C. I., Hines, M. L., Hämmäläinen, M., & Jones, S. R. (2020). Human Neocortical
1011 Neurosolver (HNN), a new software tool for interpreting the cellular and network
1012 origin of human MEG/EEG data. *ELife*, 9, e51214.
1013 <https://doi.org/10.7554/eLife.51214>
- 1014 Penfield, W., & Boldrey, E. (1937). Somatic motor and sensory representation in the
1015 cerebral cortex of man studied by electrical stimulation. *Brain*, 60(4), 389–443.
1016 <https://doi.org/10.1093/brain/60.4.389>

- 1017 Pogosyan, A., Gaynor, L. D., Eusebio, A., & Brown, P. (2009). Boosting Cortical Activity at
1018 Beta-Band Frequencies Slows Movement in Humans. *Current Biology*, *19*(19), 1637–
1019 1641. <https://doi.org/10.1016/j.cub.2009.07.074>
- 1020 Precht, J. C., Bullock, T. H., & Kleinfeld, D. (2000). Direct evidence for local oscillatory
1021 current sources and intracortical phase gradients in turtle visual cortex. *Proceedings*
1022 *of the National Academy of Sciences*, *97*(2), 877–882.
1023 <https://doi.org/10.1073/pnas.97.2.877>
- 1024 Quinn, A. J., van Ede, F., Brookes, M. J., Heideman, S. G., Nowak, M., Seedat, Z. A., Vidaurre,
1025 D., Zich, C., Nobre, A. C., & Woolrich, M. W. (2019). Unpacking Transient Event
1026 Dynamics in Electrophysiological Power Spectra. *Brain Topography*, *32*(6), 1020–
1027 1034. <https://doi.org/10.1007/s10548-019-00745-5>
- 1028 Riehle, A., Wirtsohn, S., Grün, S., & Brochier, T. (2013). Mapping the spatio-temporal
1029 structure of motor cortical LFP and spiking activities during reach-to-grasp
1030 movements. *Frontiers in Neural Circuits*, *7*. <https://doi.org/10.3389/fncir.2013.00048>
- 1031 Roberts, J. A., Gollo, L. L., Abeyesuriya, R. G., Roberts, G., Mitchell, P. B., Woolrich, M. W., &
1032 Breakspear, M. (2019). Metastable brain waves. *Nature Communications*, *10*(1),
1033 1056. <https://doi.org/10.1038/s41467-019-08999-0>
- 1034 Rosner, B. (1983). Percentage Points for a Generalized ESD Many-Outlier Procedure.
1035 *Technometrics*, *25*(2), 9.
- 1036 Rubino, D., Robbins, K. A., & Hatsopoulos, N. G. (2006). Propagating waves mediate
1037 information transfer in the motor cortex. *Nature Neuroscience*, *9*(12), 1549–1557.
1038 <https://doi.org/10.1038/nn1802>
- 1039 Rule, M. E., Vargas-Irwin, C., Donoghue, J. P., & Truccolo, W. (2018). Phase reorganization
1040 leads to transient β -LFP spatial wave patterns in motor cortex during steady-state

- 1041 movement preparation. *Journal of Neurophysiology*, *119*(6), 2212–2228.
- 1042 <https://doi.org/10.1152/jn.00525.2017>
- 1043 Seedat, Z. A., Quinn, A. J., Vidaurre, D., Liuzzi, L., Gascoyne, L. E., Hunt, B. A. E., O’Neill, G. C.,
- 1044 Pakenham, D. O., Mullinger, K. J., Morris, P. G., Woolrich, M. W., & Brookes, M. J.
- 1045 (2020). The role of transient spectral ‘bursts’ in functional connectivity: A
- 1046 magnetoencephalography study. *NeuroImage*, *209*, 116537.
- 1047 <https://doi.org/10.1016/j.neuroimage.2020.116537>
- 1048 Sherman, M. A., Lee, S., Law, R., Haegens, S., Thorn, C. A., Hämäläinen, M. S., Moore, C. I., &
- 1049 Jones, S. R. (2016). Neural mechanisms of transient neocortical beta rhythms:
- 1050 Converging evidence from humans, computational modeling, monkeys, and mice.
- 1051 *Proceedings of the National Academy of Sciences*, *113*(33), E4885–E4894.
- 1052 <https://doi.org/10.1073/pnas.1604135113>
- 1053 Shin, H., Law, R., Tsutsui, S., Moore, C. I., & Jones, S. R. (2017). The rate of transient beta
- 1054 frequency events predicts behavior across tasks and species. *eLife*, *6*, e29086.
- 1055 <https://doi.org/10.7554/eLife.29086>
- 1056 Sporn, S., Hein, T., & Herrojo Ruiz, M. (2020). Alterations in the amplitude and burst rate of
- 1057 beta oscillations impair reward-dependent motor learning in anxiety. *eLife*, *9*,
- 1058 e50654. <https://doi.org/10.7554/eLife.50654>
- 1059 Sreekumar, V., Wittig, J. H., Chapeton, J. I., Inati, S. K., & Zaghoul, K. A. (2020). *Low*
- 1060 *frequency traveling waves in the human cortex coordinate neural activity across*
- 1061 *spatial scales* [Preprint]. Neuroscience. <https://doi.org/10.1101/2020.03.04.977173>
- 1062 Stolk, A., Brinkman, L., Vansteensel, M. J., Aarnoutse, E., Leijten, F. S., Dijkerman, C. H.,
- 1063 Knight, R. T., de Lange, F. P., & Toni, I. (2019). Electrocorticographic dissociation of

- 1064 alpha and beta rhythmic activity in the human sensorimotor system. *ELife*, 8,
1065 e48065. <https://doi.org/10.7554/eLife.48065>
- 1066 Swadlow, & Waxman. (2012). Axonal conduction delays. *Scholarpedia*, 7(1451).
- 1067 Takahashi, K., Kim, S., Coleman, T. P., Brown, K. A., Suminski, A. J., Best, M. D., &
1068 Hatsopoulos, N. G. (2015). Large-scale spatiotemporal spike patterning consistent
1069 with wave propagation in motor cortex. *Nature Communications*, 6(1), 7169.
1070 <https://doi.org/10.1038/ncomms8169>
- 1071 Takahashi, K., Saleh, M., Penn, R. D., & Hatsopoulos, N. G. (2011). Propagating Waves in
1072 Human Motor Cortex. *Frontiers Human Neuroscience*, 5.
1073 <https://doi.org/10.3389/fnhum.2011.00040>
- 1074 Tinkhauser, G., Pogosyan, A., Little, S., Beudel, M., Herz, D. M., Tan, H., & Brown, P. (2017).
1075 The modulatory effect of adaptive deep brain stimulation on beta bursts in
1076 Parkinson's disease. *Brain*, 140(4), 1053–1067.
1077 <https://doi.org/10.1093/brain/awx010>
- 1078 Tinkhauser, G., Pogosyan, A., Tan, H., Herz, D. M., Kühn, A. A., & Brown, P. (2017). Beta burst
1079 dynamics in Parkinson's disease OFF and ON dopaminergic medication. *Brain*,
1080 140(11), 2968–2981. <https://doi.org/10.1093/brain/awx252>
- 1081 Troebinger, L., López, J. D., Lutti, A., Bradbury, D., Bestmann, S., & Barnes, G. (2014). High
1082 precision anatomy for MEG. *NeuroImage*, 86, 583–591.
1083 <https://doi.org/10.1016/j.neuroimage.2013.07.065>
- 1084 Van Veen, B. D., & Buckley, K. M. (1988). Beamforming: A versatile approach to spatial
1085 filtering. *IEEE ASSP Magazine*, 5(2), 4–24. <https://doi.org/10.1109/53.665>
- 1086 Vidaurre, D., Hunt, L. T., Quinn, A. J., Hunt, B. A. E., Brookes, M. J., Nobre, A. C., & Woolrich,
1087 M. W. (2018). Spontaneous cortical activity transiently organises into frequency

- 1088 specific phase-coupling networks. *Nature Communications*, 9(1), 2987.
- 1089 <https://doi.org/10.1038/s41467-018-05316-z>
- 1090 Wessel, J. R. (2020). β -Bursts Reveal the Trial-to-Trial Dynamics of Movement Initiation and
- 1091 Cancellation. *The Journal of Neuroscience*, 40(2), 411–423.
- 1092 <https://doi.org/10.1523/JNEUROSCI.1887-19.2019>
- 1093 Woolrich, M., Hunt, L., Groves, A., & Barnes, G. (2011). MEG beamforming using Bayesian
- 1094 PCA for adaptive data covariance matrix regularization. *NeuroImage*, 57(4), 1466–
- 1095 1479. <https://doi.org/10.1016/j.neuroimage.2011.04.041>
- 1096 Zich, C., Quinn, A. J., Mardell, L. C., Ward, N. S., & Bestmann, S. (2020). Dissecting Transient
- 1097 Burst Events. *Trends in Cognitive Sciences*, 24(10), 784–788.
- 1098 <https://doi.org/10.1016/j.tics.2020.07.004>
- 1099 Zich, C., Woolrich, M. W., Becker, R., Vidaurre, D., Scholl, J., Hinson, E. L., Josephs, L.,
- 1100 Braeutigam, S., Quinn, A. J., & Stagg, C. J. (2018). *Motor learning shapes temporal*
- 1101 *activity in human sensorimotor cortex* [Preprint]. Neuroscience.
- 1102 <https://doi.org/10.1101/345421>
- 1103

Supplemental Information

Spatiotemporal organization of human sensorimotor beta burst activity

Catharina Zich, Andrew J Quinn, James J Bonaiuto, George O'Neill, Lydia C Mardell, Nick S Ward, Sven Bestmann

Supplemental Methods

Burst threshold

Detecting bursts simultaneously in the temporal, spectral and spatial domain is accompanied by some conceptual and computational challenges. Here we opt for a simple thresholding approach, rather than a more data driven approach, such as the Hidden Markov Model (HMM, (Quinn et al., 2019; Vidaurre et al., 2016)). Firstly, existing HMM variants do not provide the here desired frequency resolution. Secondly, adapting the amplitude-envelope HMM to threshold power derived from time-frequency analysis poses a computational challenge for this high-dimensional dataset. Finally, one of the main advantages of HMM, i.e., the prevention of burst-splits (see (Quinn et al., 2019)), is overcome in the 5D clustering procedure. Together, while HMM, and other data driven approaches are generally advantageous, in this framework a simple amplitude threshold is preferred.

Another aspect worth highlighting affects the threshold to detect bursts, which can be summarised as follows: Are bursts better binarised by using a uniform or adaptive threshold across time, frequency, and space? Here we opt for the former approach, as it allows for direct comparisons across different points in time, frequency, or space. On the other hand, the latter has the potential of accounting for differences in SNR across time, frequency, and space.

5D clustering

To obtain 3D bursts, binarized data were clustered using a three-stage approach (see **Supplemental Video 1**). Note that data are 4-dimensional, i.e., time x frequency x space x trial, whereby space is on its own 3-dimensional (x, y, z coordinates of surface locations).

First, for each trial data were clustered in 2D (i.e., time x frequency). To this end, the binarized data were summed over the spatial domain and time-frequency cells with at least one surface

location being 'on' were clustered using 8-connectivity (i.e., connected horizontally, vertically, or diagonally).

Second, for each time-frequency cell with at least one surface location being 'on', spatial locations on the surface mesh were clustered in 3D (i.e., x, y, z coordinates of surface locations). Spatial locations were part of the same cluster if their Euclidean distance was smaller than the maximal distance of two spatial locations ($M = 2.66\text{mm}$; $SD = 0.15\text{mm}$ across individuals).

Finally, source clusters were combined across time-frequency cells using 8-connectivity, i.e., if two spatial clusters of two adjoining time-frequency cells overlapped in at least one surface location the two spatial clusters were combined. This procedure allows clustering in high-dimensional irregular space and results in 3D (time x frequency x space) bursts.

Propagation speed

Propagation speed was calculated by dividing the distance between the spatial locations with the largest and smallest relative latency (i.e., latency of each surface location relative to the average latency) by the difference in their latencies (Bahramisharif et al., 2013). Distance can be computed either on the original surface or on the inflated surface (**Supplemental Fig. 9**). The speed computed using the distance on the original surface ($M = 4.90\text{m/s}$, $SD = 0.46\text{m/s}$ across individuals) is faster than the speed computed using the distance on the inflated surface ($M = 2.61\text{m/s}$, $SD = 0.39\text{m/s}$ across individuals). This difference is well in line with a suggested cortical folding factor of x2.2 to adjust propagation speeds for cortical folding (Alexander et al., 2016; Burkitt et al., 2000). Propagation speed is in the expected range of macroscopic waves (Hughes, 1995; Muller et al., 2018).

References

- Alexander, D. M., Nikolaev, A. R., Jurica, P., Zvyagintsev, M., Mathiak, K., & van Leeuwen, C. (2016). Global Neuromagnetic Cortical Fields Have Non-Zero Velocity. *PLOS ONE*, *11*(3), e0148413. <https://doi.org/10.1371/journal.pone.0148413>
- Bahramisharif, A., van Gerven, M. A. J., Aarnoutse, E. J., Mercier, M. R., Schwartz, T. H., Foxe, J. J., Ramsey, N. F., & Jensen, O. (2013). Propagating Neocortical Gamma Bursts Are Coordinated by Traveling Alpha Waves. *Journal of Neuroscience*, *33*(48), 18849–18854. <https://doi.org/10.1523/JNEUROSCI.2455-13.2013>
- Burkitt, G. R., Silberstein, R. B., Cadusch, P. J., & Wood, A. W. (2000). Steady-state visual evoked potentials and travelling waves. *Clinical Neurophysiology*, *111*(2), 246–258. [https://doi.org/10.1016/S1388-2457\(99\)00194-7](https://doi.org/10.1016/S1388-2457(99)00194-7)
- Hughes, J. R. (1995). The Phenomenon of Travelling Waves: A Review. *Clinical Electroencephalography*, *26*(1), 1–6. <https://doi.org/10.1177/155005949502600103>

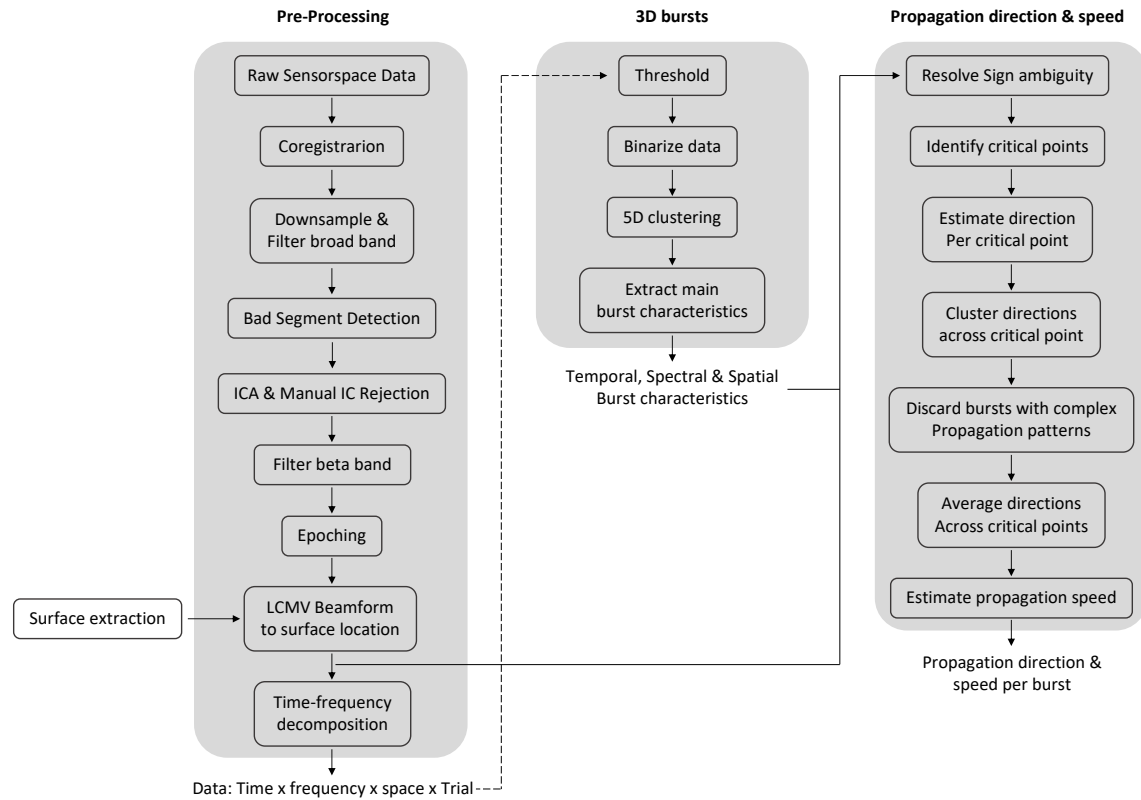
- Muller, L., Chavane, F., Reynolds, J., & Sejnowski, T. J. (2018). Cortical travelling waves: Mechanisms and computational principles. *Nature Reviews Neuroscience*, *19*(5), 255–268. <https://doi.org/10.1038/nrn.2018.20>
- Quinn, A. J., van Ede, F., Brookes, M. J., Heideman, S. G., Nowak, M., Seedat, Z. A., Vidaurre, D., Zich, C., Nobre, A. C., & Woolrich, M. W. (2019). Unpacking Transient Event Dynamics in Electrophysiological Power Spectra. *Brain Topography*, *32*(6), 1020–1034. <https://doi.org/10.1007/s10548-019-00745-5>
- Vidaurre, D., Quinn, A. J., Baker, A. P., Dupret, D., Tejero-Cantero, A., & Woolrich, M. W. (2016). Spectrally resolved fast transient brain states in electrophysiological data. *NeuroImage*, *126*, 81–95. <https://doi.org/10.1016/j.neuroimage.2015.11.047>

Supplemental Video 1

Same as Fig. 2, but each frame corresponds to a different critical point within the burst.

Supplemental Fig. 1

A schematic for the processing pipeline.

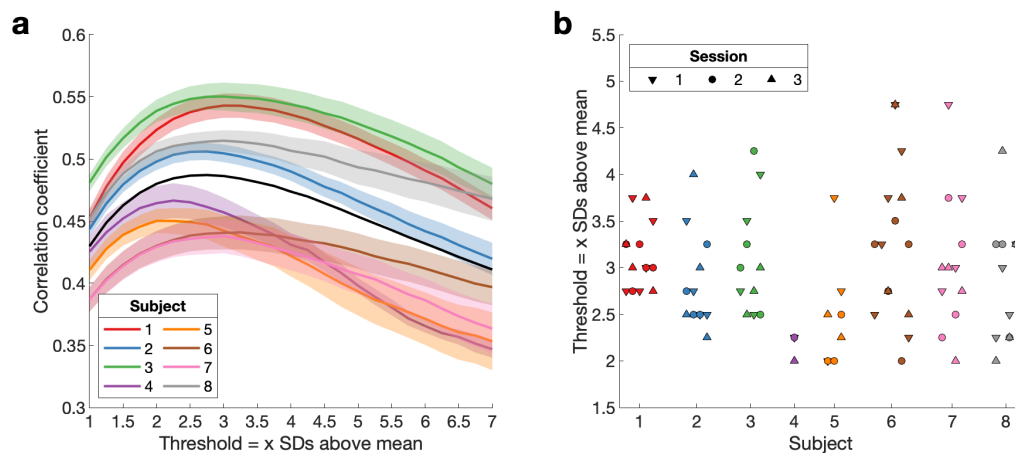


Supplemental Fig. 2

Empirical threshold to binarize beta bursts. To account for difference in signal-to-noise across sessions, days and subjects we obtained one threshold per session.

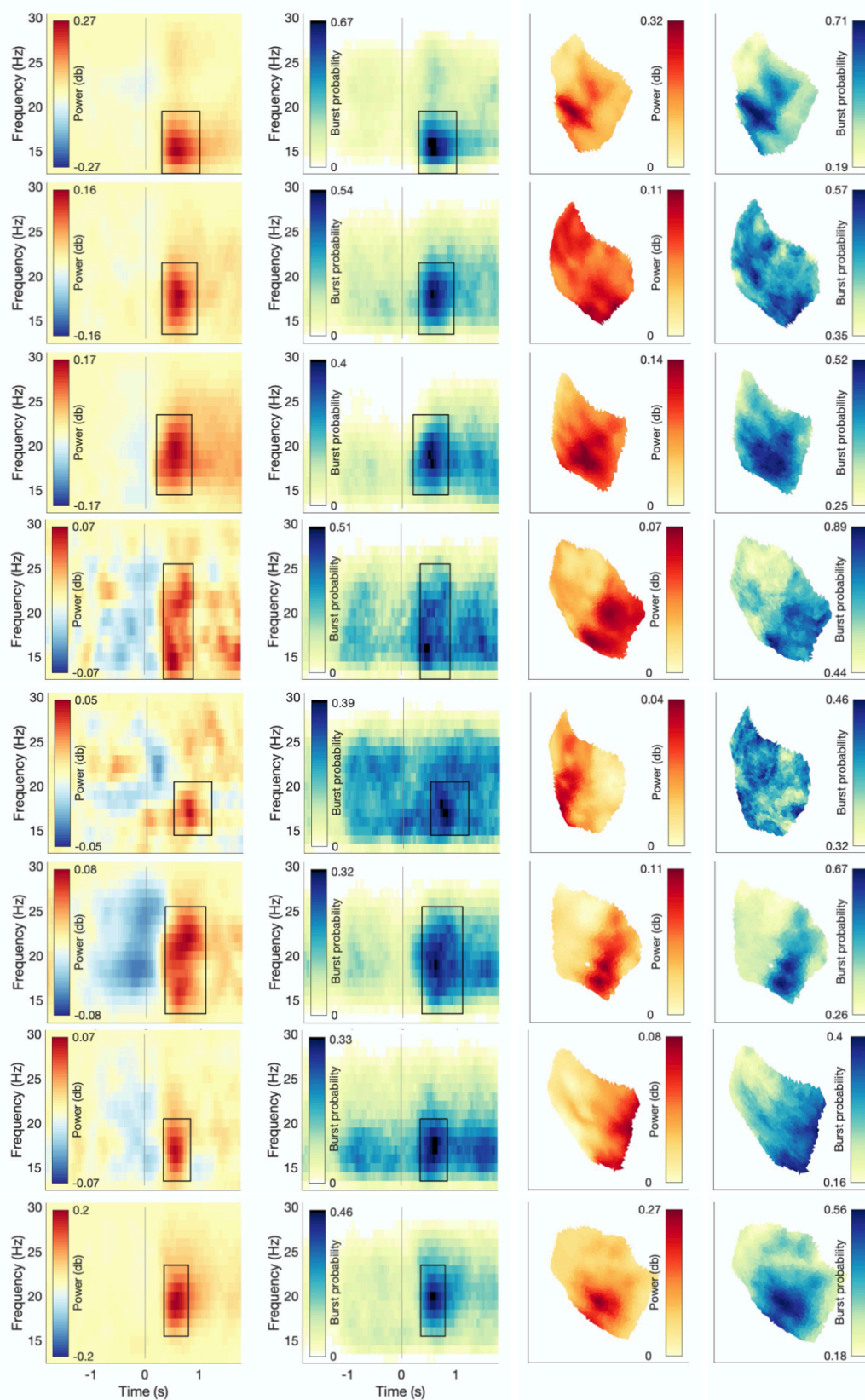
(a) Mean correlation curves across days for each subject and sessions (+/- SEM) and across subjects (black line).

(b) Empirical threshold for each session.



Supplemental Fig. 3

Beta power and burst probability are shown for all three signal domains for each subject. (left) Conventional beta power and burst probability are shown as a function of time and frequency. To this end, data are averaged across the ROI. (right) Conventional beta power and burst probability as a function of space averaged in time and frequency (indicated by the rectangle in the time-frequency plot)



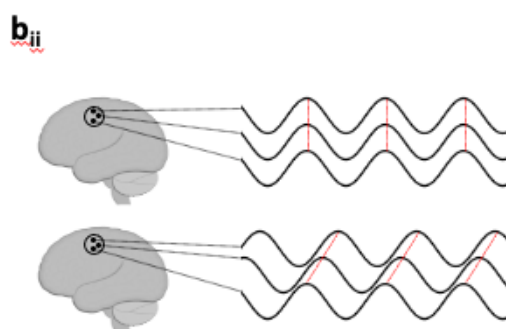
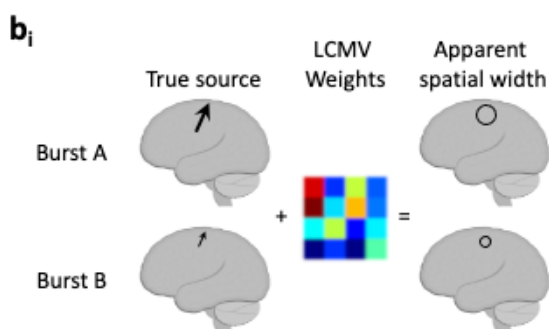
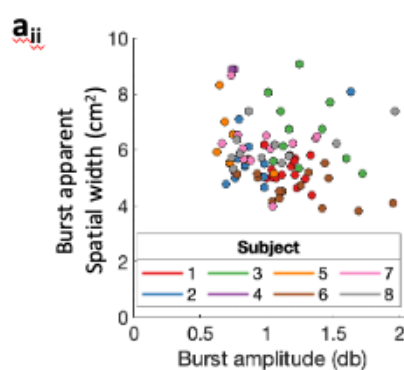
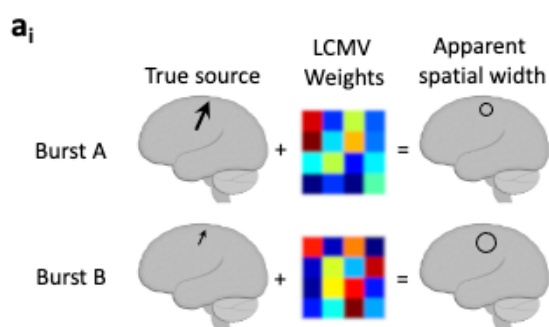
Supplemental Fig. 4

ai) Schematic illustration of how differences in SNR across sessions could theoretically explain variability in bursts' apparent spatial width. Burst A (high amplitude) and burst B (low amplitude) each with distinct LCMV weights. If SNR across sessions explains the variability in bursts' apparent spatial width, the apparent spatial width should be larger for small amplitude bursts.

aii) Relationship between burst amplitude and burst apparent spatial width across sessions within and across subjects.

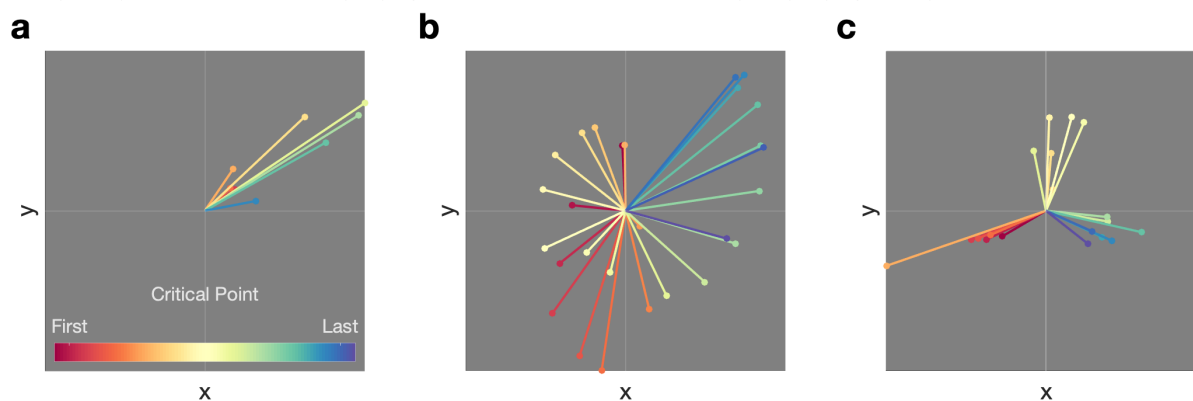
bi) Schematic illustration of how differences in SNR within a session could theoretically explain variability in bursts' apparent spatial width. Burst A (high amplitude) and burst B (low amplitude) with shared LCMV weights. If SNR within a session explains the variability in bursts' apparent spatial width, the apparent spatial width should be larger for high amplitude bursts.

bii) If bursts' apparent spatial width is merely modulated by differences in SNR across bursts within a session, 1) a positive relationship between burst amplitude and burst apparent spatial width within sessions would be present, and 2) systematic phase differences across different spatial locations within each burst should be absent. Regarding the latter, if bursts' apparent spatial width arises merely from amplitude scaling of a single source neural activity would show the same phase across different spatial locations of the burst (top). In turn, systematic phase lags across different spatial locations within the burst (bottom, Fig. 5) indicate that bursts' apparent spatial width is unlikely to arise merely from amplitude scaling of a single source.



Supplemental Fig. 5

Examples of bursts with (a) one propagation direction and (b, c) complex propagation patterns.



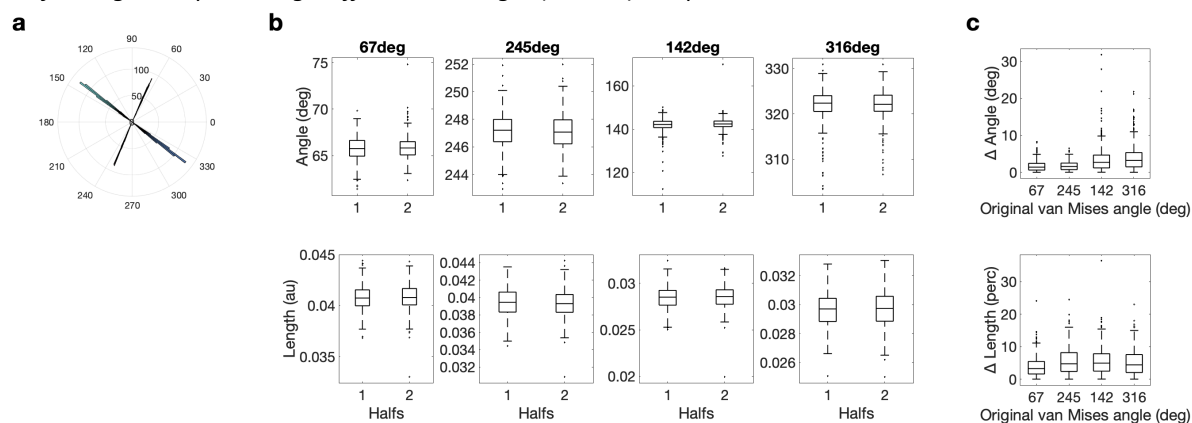
Supplemental Fig. 6

Length and angle are highly replicable for all four von Mises functions across halves of the data.

(a) Histogram of the four van Mises functions across repetitions and halves.

(b) Split-half reliability for angle (top) and length (bottom) for each van Mises function.

(c) Difference between the two halves for all four van Mises functions. For angle the angular difference (top) and for length the percentage difference in length (bottom) is reported.

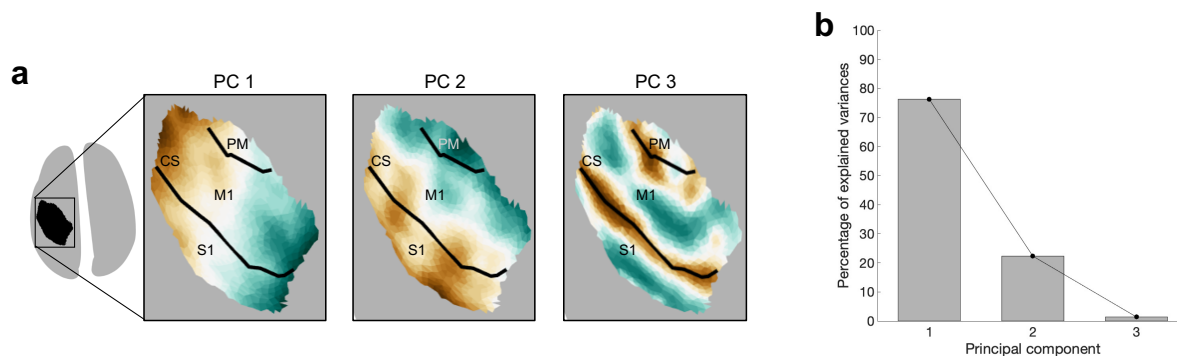


Supplemental Fig. 7

The spatial location of a burst can be summarized by the first two Principal Components (PCs) of the Cartesian coordinates of the centre of the burst.

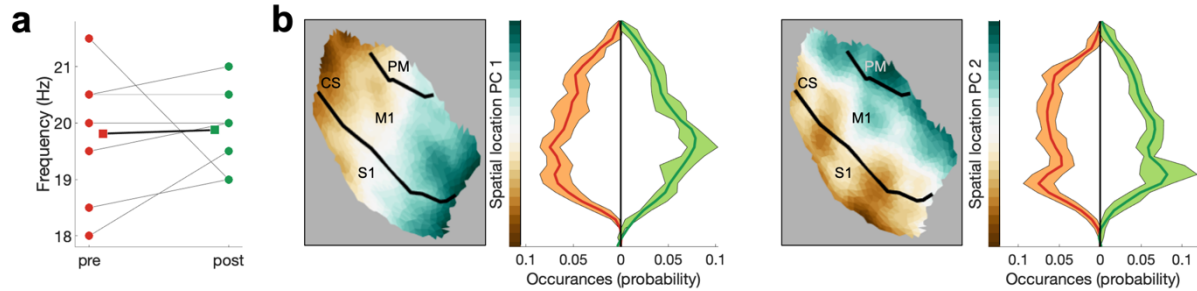
(a) For each PC the surface plot of the component structure is shown. CS, Central Sulcus. S1, Primary Sensory Cortex. M1, Primary Motor Cortex. PM, Premotor Cortex.

(b) Variance explained by each principal component.



Supplemental Fig. 8

Frequency centre (a) and spatial location (b) and were not significantly different between pre-movement (red) and post-movement (green) bursts. CS, Central Sulcus. S1, Primary Sensory Cortex. M1, Primary Motor Cortex. PM, Premotor Cortex.

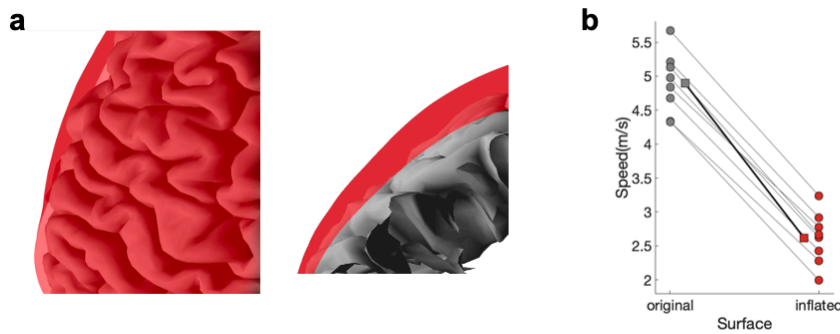


Supplemental Fig. 9

Propagation speed using the distance on the original or the inflated surface.

(a) Overlay of the original (grey) and inflated surface (red).

(b) Medians are shown for each subject (circles) and the mean across the subjects' medians (square).



Supplemental Fig. 10

Reducing temporal duration, frequency spread and apparent spatial width to burst extend using Principal Component Analysis (PCA).

(a) Temporal duration, frequency spread, and apparent spatial width are highly correlated across bursts. Coloured lines represent the least-squares fit for each subject and shaded areas indicate 95% confidence intervals.

(b) Correlation matrix, whereby the Pearson correlation is averaged across subjects within each cell.

(c) Variance explained by each principal component.

